Proceedings of the 4th BSME-ASME International Conference on Thermal Engineering
27-29 December, 2008, Dhaka, Bangladesh

NUMERICAL STUDY OF TURBULENT SLOT-JET IMPINGEMENT HEAT TRANSFER FROM CONCAVE CYLINDRICAL SURFACES

M.A.R. Sharif and K.K. Mothe
Aerospace Engineering and Mechanics Department, The University of Alabama
Tuscaloosa, Alabama 35487-0280, U.S.A., msharif@eng.ua.edu

ABSTRACT

Numerical investigation of convective heat transfer process from concave cylindrical surfaces due to turbulent slot-jet impingement is performed. Constant heat flux condition is specified at the concave surfaces. The flow and thermal fields in the vicinity of the surfaces are computed using the RNG $k-\varepsilon$ turbulence model with a two layer near wall treatment. Parametric studies are carried out for various jet exit Reynolds numbers, surface curvature, and nozzle-to-surface spacing. Results presented include streamlines, isotherms, and the Nusselt number distribution on the impingement concave wall for various parameter values in the study. The results indicate that while the jet exit Reynolds number and the surface curvature have a significant effect on the heat transfer process, it is relatively insensitive to the jet-to-target spacing. A correlation for the average Nusselt number at the concave surface as a function of the parameters considered in the study is also derived.

KEY WORDS: *Numerical simulation, slot-jet impingement, concave surface, RNG $k-\varepsilon$ model.*

1. INTRODUCTION

Due to high rates of localized heat transfer, impinging jet flows are employed in a wide variety of applications of practical interest. Even though the flow geometry is simple in jet impingement heat transfer problems, the physics of the flow is very complex due to the shear layer development at the free jet and wall jet boundaries, boundary layer development at the impingement surface, and very high streamline curvature near the impingement location. The flow physics of jets impinging on flat surfaces is significantly altered when the impingement occurs on a curved surface. The surface curvature has a strong effect on the overall flow as well as in the wall jet development in the circumferential direction due to the additional streamline curvature and associated centrifugal and Coriolis forces.

There has been several experimental investigation of jet impingement on curved surfaces in the past which include the cases of impingement on concave and convex surfaces. Recently Choi et al. [1] experimentally investigated slot-jet impingement cooling of semi-circular concave surfaces and presented the thermal and hydrodynamic data for different Reynolds numbers and nozzle-to-surface distances. On the other hand, papers on numerical investigation of turbulent jet impingement heat transfer from curved surfaces is not plentiful in the literature. Yang and Hwang [2] numerically investigated the hydrodynamics of turbulent slot jet impingement on convex semi-cylindrical surfaces without any heat transfer consideration. Souris and Liakos [3] have done numerical studies on impingement cooling on concave cylindrical surfaces using the standard $k-\varepsilon$ model and the Reynolds stress transport model along with the non-equilibrium wall function [4] for both models. They compared their predictions with the experimental data of Choi et al. [1] and found a satisfying

agreement between the numerical prediction and experimental data using both turbulence models. Hu and Zhang [5], conducted numerical investigation in addition to the experimental measurement for circular water jet impingement heat transfer from a convex hemispherical surface. They, however, did not report which turbulence model was used in the computation, if any.

In the present work, a parametric study of the slot jet impingement on concave cylindrical surfaces is conducted for a wide range of flow and geometric parameters. The geometric configuration is chosen based on the experimental setup of Choi et al. [1] so that the code validation can be performed against their experimental data. The results of the parametric study are presented in terms of the streamline and isotherm plots, and the Nusselt number at the heated surface. A correlation for the average Nusselt number for impinging flows over concave surfaces has also been derived as a function of the parameters.

2. MATHEMATICAL FORMULATION AND NUMERICAL METHOD

The Reynolds averaged mass, momentum, and energy conservation equations for the steady incompressible flow, neglecting the viscous dissipation, are solved. The computations in this study are performed using the Fluent version 6.3 commercial flow solver code [6] utilizing the RNG $k-\varepsilon$ turbulence model [7] for the closure and a two-layer enhanced wall treatment. The flow domain is divided into many small finite volumes with an unstructured mesh. A collocated arrangement for the placement of the flow variables is used in the mesh system. The nonlinear conservation equations for mass, momentum, and energy and other transport equations are integrated over each of the finite volume to yield sets of linear algebraic equations which are then solved sequentially using an iterative method. The SIMPLE algorithm [8] is used for pressure-velocity coupling. The convective fluxes have been calculated using the second order upwind scheme while the diffusive fluxes have been calculated using the central difference scheme. The convergence is assumed when the value of the scaled residual of continuity, momentum, and energy equations is less than 10^{-6}.

3. RESULTS AND DISCUSSION

Figure 1 shows the schematic diagram of the impinging slot-jet on a semi-circular concave surface which closely resembles the experimental conditions of Choi et al. [1]. The jet is unconfined, meaning the two vertical plane surfaces and the circular surfaces around the jet bounding the domain shown in the figure are open. The variable '*a*' in the sketch represents the inward radial distance from the impingement wall while the variable '*s*' represents the distance along the circumferential direction from the impingement point.

The experimental conditions [1] consisted of a slot-jet with 5 mm width (*B*) used to produce an air jet impinging onto a semi-circular concave surface with a diameter (*D*) of 150 mm, on which a constant heat flux q_w of 5,000 W/m^2 was applied. The parametric investigations are conducted by carefully selecting a set of values for the important parameters relevant to this problem. These parameters are; *i*) the jet exit Reynolds number, Re, based on the jet exit velocity and the hydraulic diameter of the slot-jet which can be shown to be equal to 2*B*, *ii*) the normalized spacing between the nozzle exit and the impingement surface (*h/B*), and *iii*) the relative curvature of the impingement surface represented by the ratio of the surface diameter and the jet width, (*D/B*). The selected values of these parameters are; Re = 3,000, 6,000, 9,000, and 12, 000; h/B = 3, 6, 9, and 12; and D/B = 30, 40, 50, and 60. Constant fluid properties of density (1.225 kg/m^3), dynamic viscosity (1.7894×10^{-5} kg/m s), thermal conductivity (0.0242 W/m K), and specific heat at constant pressure (1006.43 W/kg K) are used for all calculations. These values correspond to a Prandtl number, Pr, of 0.744. At the jet

exit, velocity-inlet boundary condition is used with a velocity magnitude compatible to the jet exit Reynolds number. On the wall, the no-slip wall boundary condition with constant heat flux value (5,000 W/m^2) is set. At all other open surfaces, constant pressure-outlet condition is used.

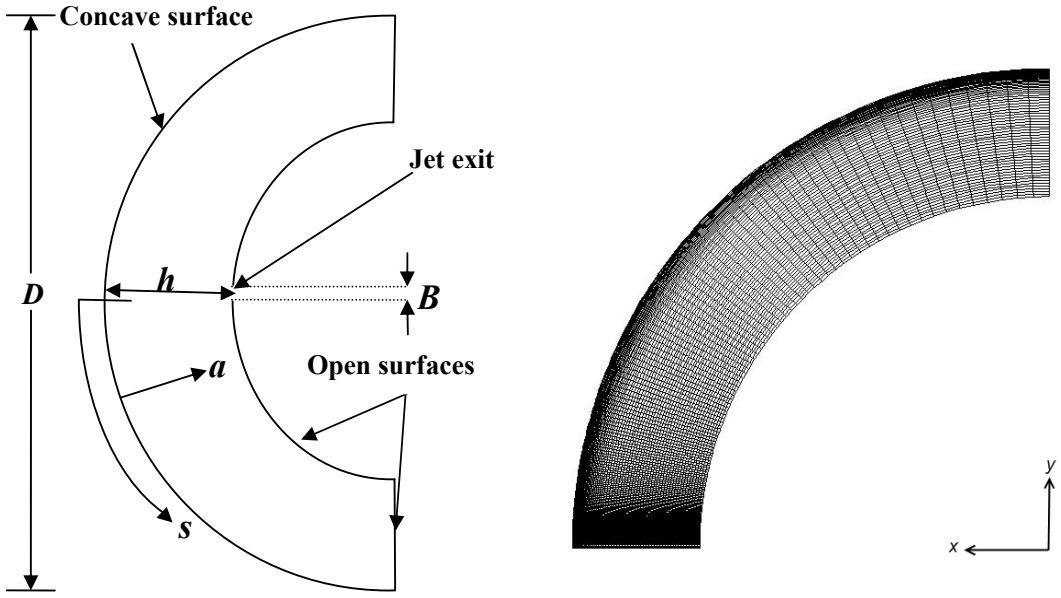

Fig. 1. Schematic diagram of the slot-jet impingement on a concave cylindrical surface and a sample mesh.

The streamlines of the flow of jet impinging on a concave surface for some representative cases are presented in Figure 2. The representative cases chosen are for *D/B* =30, *h/B* = 3 and 12, and Re = 6,000 and 12,000. It can be seen in these streamline plots that after impingement the jet gradually transforms into wall jet along the concave surface. The development of the boundary layer and the shear layer and their gradual spread is clearly discernible in these plots. The boundary and shear layer thickness in the wall jet region increases as the jet to surface spacing (*h*/*B*) is increased for a particular Reynolds number.

The isotherm plots for the same representative cases are shown in Figure 3. The isotherms are for the non-dimensional temperature θ defined as $(T - T_j)/\Delta T$ where T_j is the jet exit temperature and $\Delta T = q_w(2B)/k$, k being the thermal conductivity of the fluid. It can be seen from Figure 3 that the thermal boundary layer thickness increases as we move away from the stagnation point along the circumferential direction. Very steep temperature gradients at the impingement region is noticed which is responsible for the high local Nusselt number there.

The local Nusselt number variation for a few representative cases are shown in Figure 4 for *D/B* = 30. These plots show the significant effect of the jet exit Reynolds number on the local Nusselt number variation at any combination of *D/B* and *h/B*. This can be attributed to the fact that the convection strength and turbulence level increases with increasing Reynolds number which in turn enhances heat transfer. The Nusselt number is highest in the impingement region (*s*/*B* ~ 0) at any configuration and at any Reynolds number. However, the peak of the Nusselt number occurs slightly downstream from the stagnation point (*s*/*B* = 0) from where the Nusselt number decreases monotonically.

The overall effectiveness of the heat transfer process due to jet impingement on the heated concave surface can be quantified by the average Nusselt number which is obtained by integrating the local Nusselt number distribution along the surface and then dividing the integral by the total arc length of the impingement surface. This is calculated for all of the configurations used in this study. The variation of the average Nusselt number is shown in Figure 5 as a function of the Reynolds number for different combinations of D/B and h/B. The average Nusselt number increases almost linearly with Reynolds number for any specific combination of D/B and h/B. It is also more sensitive to the separation distance for higher relative curvature (lower values of D/B) but is somewhat insensitive as the surface curvature flattens (higher D/B values) especially at lower Reynolds number. This is consistent with the previous discussion on the local Nusselt number distribution at the heated surface.

A correlation expressing the relationship between the average Nusselt number and the other relevant parameters is obtained form the numerical results as

$$\overline{\mathrm{Nu}} = 0.107\,\mathrm{Re}^{0.761}\left(D/B\right)^{-0.346}\left(h/B\right)^{-0.047} \tag{11}$$

The separation parameter (h/B) has a rather weak effect on the average Nusselt number since its exponent is much smaller compared to that of the other parameters. Also the average Nusselt number varies inversely with the surface curvature and spacing (negative exponent) and directly with the Reynolds number (positive exponent).

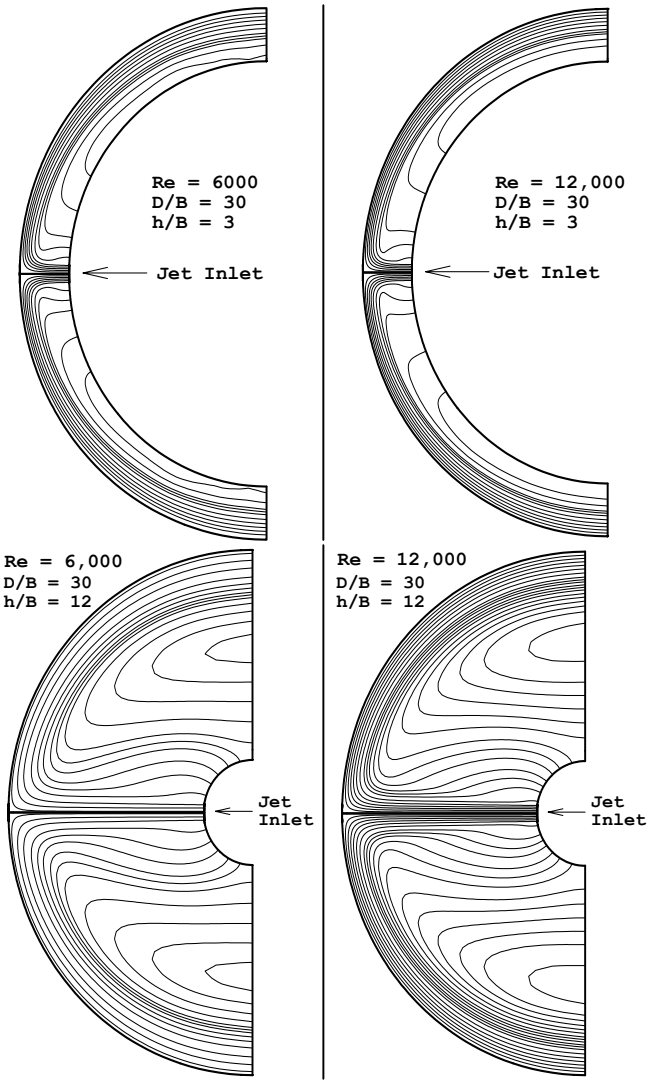

Fig. 2. Some representative streamline plots in the flow domain.

4. CONCLUSIONS

Parametric study of turbulent slot-jet impingement heat transfer from concave cylindrical surfaces heated with constant heat flux condition is performed. The hydrodynamic and thermal field is computed using the RNG $k-\varepsilon$ model with the two layer enhanced wall treatment approach. The major conclusions of this parametric study are;

i) The Reynolds number has a significant effect on the heat transfer process. The local Nusselt number at the heated surface significantly increases at any particular circumferential location with increasing Reynolds number for any set of jet-to-target spacing and relative curvature.

ii) The local Nusselt number distribution starts with a high value at the stagnation point with a peak at a slightly offset location from the stagnation point and then quickly and monotonically decreases along the heated surface.
iii) The local Nusselt number distribution is not very sensitive to the jet-to-target spacing at higher relative curvature (D/B) values.
iv) The surface curvature has significant effect on the local and average Nusselt number when the curvature is strong, i.e., at lower D/B values.
v) The average Nusselt number at the heated surface increases almost linearly with the Reynolds number.

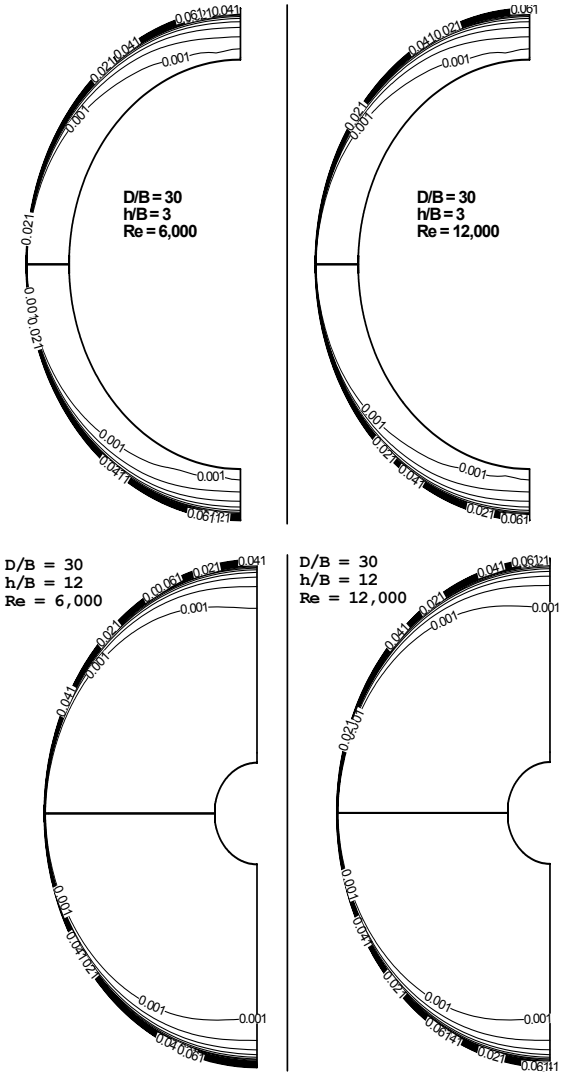

Fig. 3. Some representative isotherm plots in the flow domain.

REFERENCES

1. M. Choi, H.S. Yoo, G. Yang, J.S. Lee, D.K. Sohn, Measurement of impinging jet flow and heat transfer on a semi-circular concave surface, Internat. J. Heat Mass Transfer 43 (2000) 1811.
2. Y.T. Yang, C.H. Hwang, Numerical simulations on the hydrodynamics of a turbulent slot jet impinging on a semicylindrical convex surface, Numerical Heat Transfer, Part A 46 (2004) 995-1008.
3. N. Souris, H. Liakos, Impinging jet cooling on concave surfaces, AIChE Journal 50 (2004) 1672-1683.
4. S.E. Kim, D. Choudhury, A near-wall treatment using wall functions sensitized to pressure gradient, ASME FED Vol. 217, Separated and Complex Flows, ASME, 1995.
5. G. Hu, L. Zhang, Experimental and numerical study of heat transfer with impinging circular jet on a convex hemispherical surface, Heat Transfer Engineering 28 (2007) 1008-1016.
6. Fluent CFD code, Fluent Inc., 10 Cavendish Court, Lebanon, NH 03766, www.fluent.com.
7. V. Yakhot, S.A. Orszag, S. Thangam, T.B. Gatski, C.G. Speziale, Development of turbulence models for shear flows by a double expansion technique, Physics of Fluids A 4 (1992) 1510-1520.
8. S.V. Patankar, Numerical heat transfer and fluid flow, Hemisphere Publishing Corporation, 1980.

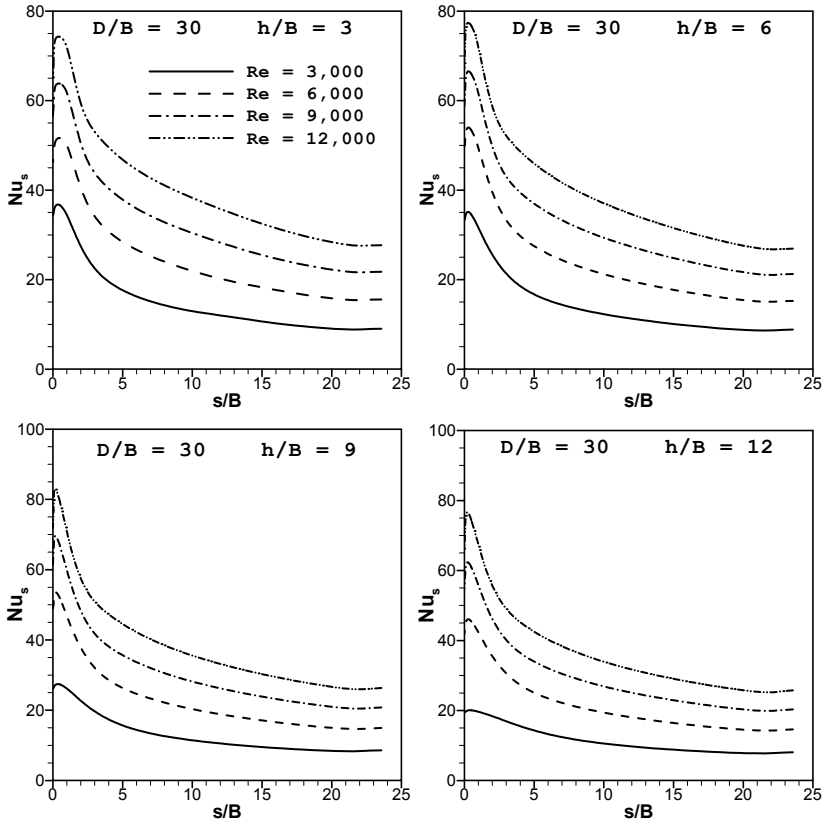

Fig. 4. Local Nusselt number variation along the concave surface for different Reynolds numbers, $D/B = 30$.

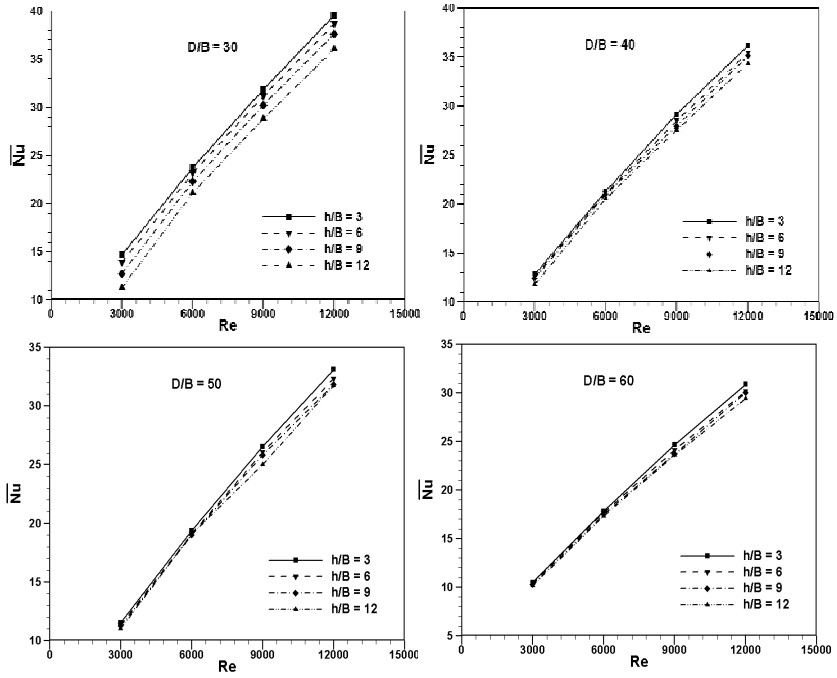

Fig. 5. Average Nusselt number at the heated concave surface.

Proceedings of the 4th BSME-ASME International Conference on Thermal Engineering
27-29 December, 2008, Dhaka, Bangladesh

EXERGETIC ANALYSIS OF COAL FIRED THERMAL POWER PLANTS BASED ADVANCE STEAM PARAMETERS

Souman RUDRA, Hyun Min SHIM and Hyung Taek KIM

Division of Energy Systems Research, Graduate School, Ajou University, Suwon 443-749, Korea.
e-mail: souman@ajou.ac.kr

ABSTRACT

Modifications are examined to increase coal-fired steam power plant efficiency by advance steam parameters. This paper presents study of coal based thermal power plant using sub-critical, supercritical and ultra-supercritical steam conditions. We consider our configuration for the power plant is about 500 MW. A version of a process-simulation computer code (ASPEN Plus) for exergy analysis is used. Overall exergy efficiency is 36% for the coal-fired process. The study also delineates the effects of condenser pressure on plant and exergy efficiency. The effect of high grade coal on performance parameters as compared to typical Bangladeshi high grade coal was also considered as the study. Exergy losses are associated with internal consumptions means coal combustion followed by the steam generator. Due to some limitations, the maximum possible plant efficiency was found to be about 40.2% for supercritical steam power plant and 44.8% for the ultra-supercritical steam power plant.

KEYWORDS: *Exergy, sub-critical, supercritical, ultra-supercritical, Bangladeshi coal.*

1. INTRODUCTION

At the present times, Coal fired thermal power plants meet the growing energy demand with least fuel (coal) consumption. It is, therefore, really needed to develop strategies for the optimization of these Systems by using advance steam parameters. Electricity in particular, plays a vital role in developing the status of life. Bangladesh has up to 2.7 billion short tons of high-quality coal reserves (Bangladesh's Energy Ministry judges, 2007) and thus coal-based thermal power plants dominate source-wise mix with hopeful installed capacity of a total capacity. The only coal fired power plants in Bangladesh is operating on sub-critical steam conditions. Exergy is the work which can be produced by a stream or system as it is brought into equilibrium with a reference environment, and can be thought of as a measure of the quality (or usefulness) of energy, work having the highest quality. Exergy is consumed during real processes, and conserved during ideal processes.

Exergy analysis of a coal-based 210MW thermal power plant was explained with different load variation [1]. Kotas and Stecco, Moran (1992) carried out exergy analysis for various systems and determined the exergy losses at each process in the system [2, 3]. Sciubba and Su had done a second law analysis of the steam turbine power cycle to analyze the influence of reheat temperature and pressure on regenerative cycle performance [4]. Applications of exergy analysis have increased in recent years, and have included investigations of coal fired electricity generation using conventional [5–8],

Exergy analysis provides insight into losses in various components of a power generating system. Unlike energy, exergy is not generally conserved but is destroyed. So, the

majority of the causes of irreversibilities like heat transfer through a finite temperature difference, chemical reactions, friction, and mixing are accounted by exergy analysis [9]. Rosen has compared the performance of operating coal-fired and nuclear steam power plant located in Canada of unit size of approximately 500 MW using a process-simulator, ASPEN Plus [10]. Chew reviewed the sensitivity of supercritical steam plant cycle performance to operating conditions [11]. Recently, Bugge et al. (2006) have presented the status and perspectives for the AD700 technology which involves the development of a coal-fired power plant with steam temperature of 700^0C [12]. An improvement in plant efficiency can be achieved by using supercritical and ultra-supercritical steam conditions. Enhanced efficiency results in reduced emission of CO_2 / unit kWh. In Bangladesh, the first coal-fired power plant began commercial production at 250 MW at Baropukuria in parbotipur in 2006 January. An attempt has been made in this paper to predict the possible improvement in efficiency obtained with thermal power plants based on advanced steam conditions in Bangladeshi climatic conditions for Barapukuria (Bangladesh) high grade coal.

2. PROCESS DESCRIPTION

Complete process flow sheets by ASPEN plus, considered 500 MW unit size coal-based power plants involving sub-critical, supercritical and ultra-supercritical steam conditions are shown in Figures 1-3 respectively. An operating pulverized coal combustion sub-critical steam power plant unit [10], Bangladesh has chosen these parameters for comparison.

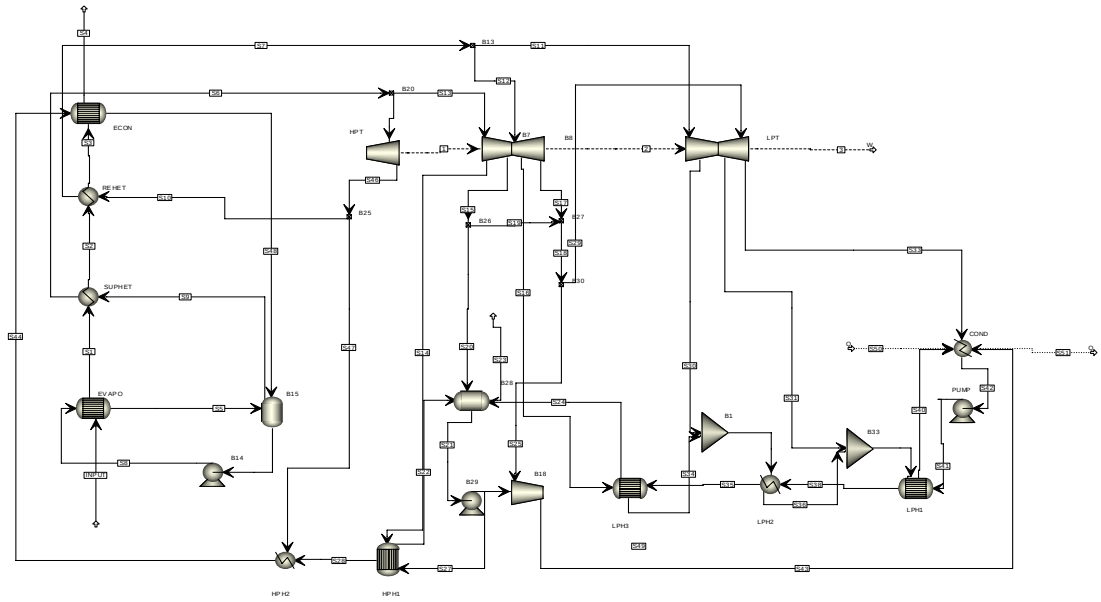

Fig.1 Flowsheet for the 500 MW subcritical steam power plant

Heat is produced and used to generate and reheat steam. In coal fired sub-critical steam power plant (Fig.1), take a assumption of natural circulation steam generators each produce 453.6 $kg.s^{-1}$ steam 174 bar and 540 ^{0}C. The plant uses a single stage reheating with the maximum feed water temperature at the inlet of economizer being 256 ^{0}C. Air is supplied to the furnace by two 1080 kW, 600-rpm motor-driven forced draft fans. And for the supercritical steam power plant shown in Fig. 2 has steam parameters of 290 bar and 582 ^{0}C with 2-stage reheating and feed water temperature of 300 at the inlet of economizer [12].

For further improvement of the plant efficiency, it's needed to operate the plant by ultra-supercritical steam. The design configuration of an ultra-supercritical thermal power plant presented by Kjaer [12] has been considered for the study. The steam parameters for the

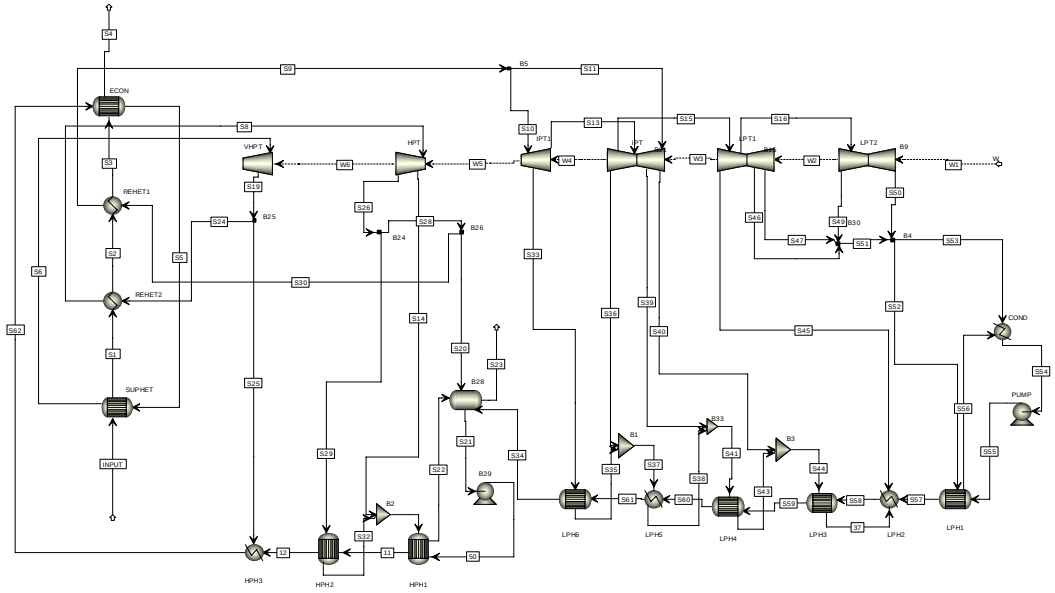

Fig.2 Flowsheet for the 500 MW supercritical steam power plant

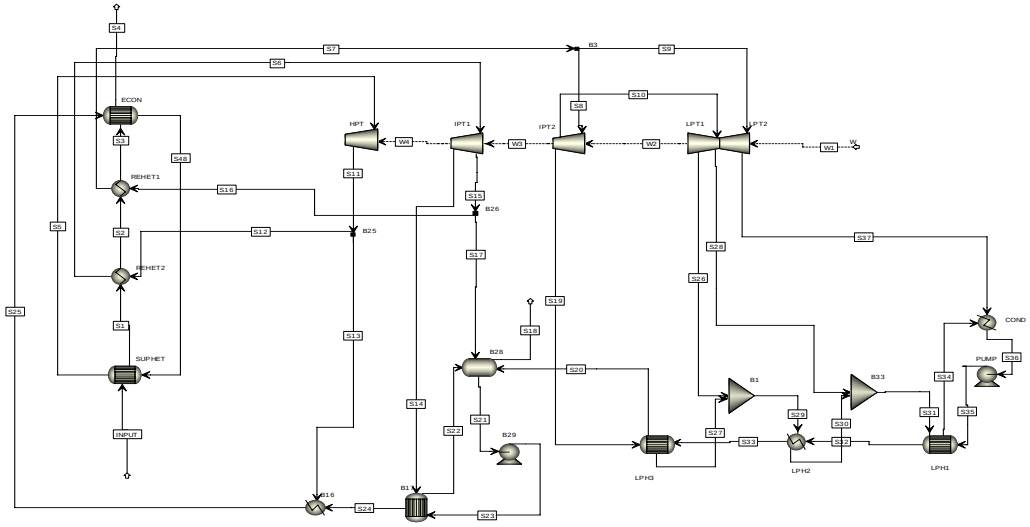

Fig.3 Flowsheet for the 500 MW ultrasupercritical steam power plant

power plant are around 375 bar and 720 ^{0}C with 2-stage reheating and feed water temperature of 350 ^{0}C at the inlet of economizer.

3. ANALYSIS

Exergy efficiency is evaluated as ratios of products to inputs. For the overall stations, the exergy efficiency is denoted by,

$$\psi = \frac{\text{Net exergy output with electricity}}{\text{Exergy input}} \tag{1}$$

For Aspen Plus simulation, some assumptions were considered for which we get better simulation results. The composition of all streams is 100% H_2O, except that, on a volume basis, the composition of Input are 79% N_2, 6% O_2 and 15% CO_2. Vapor fraction is listed as 0.0 for liquids and 1.0 for superheated vapors.

Some others assumptions:- 1). The turbines have isentropic and mechanical efficiencies of 80% and 95%, respectively; 2).The reference state for water / steam is saturated liquid at a temperature of 25 ^{0}C; 3).The incoming fuel temperature is 25 ^{0}C; 4). The kinetic and potential exergies are neglected; 6). The generators and transformers are each 99% efficient, and heat losses from their external surfaces occur at 15 ^{0}C and 7).Condenser pressure: 100 mbar.

4. COAL CHARACTERISTICS

The considered coal for this paper represents the typical coal of Bangladesh (Baropukuria coal mine) with lower heating value 22.7 MJ/Kg [13]. With a view to compare performance of the considered systems using high grade (low mineral matter) coal, a typical Indian coal (Singareni Mines - SM) having low mineral matter was also considered [14]. The main properties of the Baropukuria coal are summarized in Table 1. The chemical composition of the two different coal samples displays significant differences that can be relevant for their deposition behavior.

Table.1 Main properties of the coal

Type	Bangladesh(BM)	India(SM)
Proximate analysis (% by weight, dry basis)		
Fixed carbon	44.2	25..5
Volatile matter	24.3	31.4
Ash	21.5	43.1
Elemental analysis (% by weight)		
Carbon	77.84	38.9
Hydrogen	5.40	2.6
Nitrogen	1.68	0.7
Sulfur	0.6	0.6
Oxygen	11.20	6.7
Moisture	3.28	5.7
Mineral matter composition (% by weight)		
SiO_2	54.4	38.95
Al_2O_3	35.6	23.98
Fe_2O_3	2.9	26.52
K_2O	0.66	1.44
MgO	0.18	0.95
Na_2O	0.06	0.04
CaO	0.56	7.34
TiO_2	3.2	0.77
Mn_3O_4	0.11	-
P_2O_5	0.46	-
SO_3	0.13	-
Lower Heating Value(MJ/Kg)	22.7	14.5

It has been shown that the lower heating value of Bangladeshi Coal is better then that of Indian coal. In spite of high mineral matter, Indian coal is of high quality with regard to sulfur content which is in general less than 0.6% thus having minimal negative environmental impact.

5. SIMULATION RESULTS

Simulation and analysis data (including exergy values) for sub-critical steam power plant are summarized along with specified data in Table 2, for the streams identified in Fig. 1. Like this same procedure we can able to determine the different stream results for

supercritical and ultra-supercritical steam. The comparison of plant and exergy efficiencies of the various power plant configurations is presented in Table 3.

Table.2 Aspen Plus simulation results

Stream	Temperature(^{0}C)	Pressure(bar)	Mass flow rate (Kg.s^{-1})	Vapor friction	Exergy flow rate (MW)
Input	540	174	453.6	1.0	496.81
S1	512	142	458.8	1.0	480
S2	482	120	453.6	1.0	468.12
S4	119.44	100	710.15	1.0	62.27
S6	323.36	37.8	453.6	1.0	718.74
S7	538.00	162	453.59	1.0	718.74
S8	102	0.5	325	1.0	1.81
S9	112	1	345	1.0	4.26
S11	360.50	10.3	367.85	1.0	411.16
S15	209.93	2.15	23.88	1.0	18.82
S16	253.22	3.79	10.47	1.0	9.24
S20	360.50	10.6	26.92	1.0	30.09
S22	188.33	121	58.82	0.0	11.11
S24	124.86	10	367.85	0.0	30.41
S27	169.28	16.25	453.6	0.0	77.57
S30	108.32	68.9	12.72	1.0	7.12
S31	60.47	34.5	11.16	1.0	5.03
S33	35.63	4.5	309.62	0.93	54.07
S40	165.86	100	453.59	0.0	66.52
S41	35.63	.45	367.85	0.0	1.20
S42	35.73	100	367.85	0.0	1.70
S43	55.56	13.3	58.23	0.0	0.73
S44	228.24	16.25	453.6	0.0	131.93
S47	423.23	1.72	15.98	1.0	20.02
S50	15	1	18600	0.0	0.00
S51	24	1	18600	0.0	10.54

The results show an increase of 3.4% points in plant efficiency of supercritical power plant and almost 8% points for ultra-supercritical power plant as compared to sub-critical power plant.

Table.3 Plant and exergy efficiency of different power plant

Plant	Plant efficiency (%)	Exergy Efficiency (%)
Sub-critical	36.8	31.5
Supercritical	40.2	34.2
Ultra-supercritical	44.8	36.7

It is observed from Fig. 4, that the energy losses are associated mainly with heat rejection in cooling water and stack. The cooling water flow rate decreases from about 18,600 kg/s in the case of sub-critical power plant to 14,800 kg/s in the case of ultra-supercritical power plant for a temperature rise of 10 ^{0}C across the condenser. This is attributed to reduction in heat rejection in the condenser as the steam conditions are increased from sub-critical to supercritical. It is also observed that maximum exergy losses is due to coal combustion and the steam generator (Fig.4). The reduced losses in the steam generator can be attributed to the smaller heat transfer temperature difference as the steam parameters are increased from sub-critical to ultra-supercritical conditions. Condenser pressure directly affects the plant net power output; the corrected data is graphically shown in Fig. 5[15]. The

variation of the exergy efficiency with condenser pressure using high grade (BM) coal was studied and is also represented in Fig.5

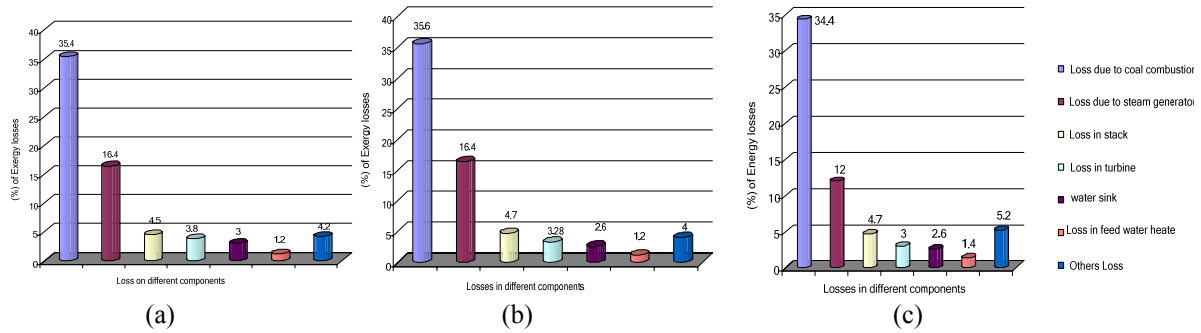

Fig.4 Exergy losses in different components for (a) sub-critical (b) supercritical and (c) ultra-supercritical steam power plant.

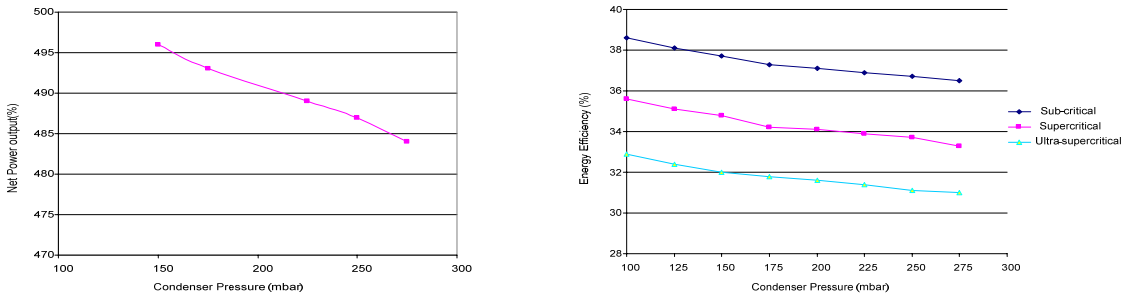

Fig.5 Comparison of net power output (MW) and exergy efficiency (%) with condenser pressure (mbar).

6. CONCLUSIONS

Coal fired thermal power plants meet the growing energy demand, and hence special attention must be given to define a strategy for the optimization of these systems. Exergy analysis presented for a coal fired thermal power plant has provided information on the irreversibilities of each process.

High grade coal from Barapukuria(Bangladesh) is appropriate for the electricity production due to its chemical properties. We have to utilize this coal for perfect manner.

Condenser pressure has little influence on the exergy efficiency. However, a reduction in condenser pressure results in an increase of the exergy efficiency. With Baropukuria (BM) coal, the exergy loss in the combustor was about 35%. In the case of steam generator, the exergy loss reduced to 12% from about 18% as the steam parameters were increased from sub-critical to supercritical conditions using this (BM) coal. Due to condenser pressure limitation, the maximum possible overall exergy efficiency was found to be about 36.7% with the ultra-supercritical power plant. Decreasing the condenser pressure by 100 mbar will increase the power output by 2.5%.Thus, installing coal-based thermal power plants based on advanced steam parameters in Bangladesh will be a prospective option aiding energy self-sufficiency.

7. ACKNOWLEDGMENTS

The research is the outcome of the fostering project of the Best Lab in the area of IGCC supported financially by the Ministry of Knowledge Economy (MKE).

8. REFERENCES

[1] S. Sengupta, A. Datta, and S. Duttagupta, Exergy analysis of a coal-based 210MW thermal power plant, Int. J. Energy Res, Wiley InterScience. 2007; 31:14–28.

[2] Kotas TJ. 1985. The Exergy Method of Thermal Plant Analysis. Butterworths: London, UK.

[3] Moran MJ, Sciubba E. 1994. Exergy analysis: principles and practice. Journal of Engineering for Gas Turbines and Power 116:285–290.

[4] Sciubba E, Su TM. 1980. Second-law analysis of the steam turbine power cycle: a parametric study. ASME Winter Annual Meeting, Computer-Aided Engineering of Exergy Systems, the Advanced Exergy System Division, vol. AES 23, Anaheim, CA, 151.

[5] R.A. Gaggioli, Available energy and exergy, International Journal of Applied Thermodynamics. 1 (1998) 1–8.

[6] M.A. Rosen, Second-law analysis: approaches and implications, International Journal Energy Res. 23 (1999) 415–429.

[7] Yasni E., Carrington C.G., The role for exergy auditing in a thermal power station, in: HTD, Vol. 80, ASME, New York, 1987, pp. 101–109.

[8] Horlock J.H., Young J.B., Manfrida G., The rational efficiency of fossil-fuel power plants, in: Proc. ASME Advanced Energy Systems Division, AES, Vol. 38, 1998, pp. 235–242.

[9] Cengel Y.A., M.A. Boles, 2004, Thermodynamics: An Engineering Approach, Tata McGraw-Hill Publishing Company Limited, New Delhi, ch.7.

[10] Rosen M.A., 2001, Energy- and exergy-based comparison of coal-fired and nuclear steam power plants, Exergy International Journal**,** 1(3), 180-192.

[11] Chew P.E., 2003, PF-fired supercritical power plant, Proc Institution Mechanical Engineers, Part A: J of Power and Energy, 217, 35-43.

[12] S. Kjaer, Advance Super Critical Power Plant, Experiences of Elsamprojekt. www.elsamprojekt.com.pl/usc.html accessed on 27th May, 2006.

[13] Baropukuria coal mining company limited, Bangladesh, www.bcmcl.org.bd .And Energy information Administration Bangladesh energy data, http://www.eia.doe.gov/emeu/cabs/Bangladesh/Electricity.html

[14] M.V.J.J. Suresh , K.S. Reddy and Ajit Kumar Kolar, Energy and exergy analysis of thermal power plants based on advance steam parameters. Advances in Energy Research (AER – 2006).

[15] C.C. Chuang, D.C. Sue, Performance effects of combined cycle power plant with variable condenser pressure and loading, Energy 30 (2005) 1793–1801.

Proceedings of the 4th BSME-ASME International Conference on Thermal Engineering
27-29 December, 2008, Dhaka, Bangladesh

PORE LEVEL MODELING OF CONVECTION IN A SILICON CARBIDE FOAM

M. Khairul Alam[1], Mihnea S. Anghelescu[1] and Matt Wright[2]
[1]Department of Mechanical Engineering, Ohio University, Athens, OH 45701, USA
[2]Ultramet, Pacoima, CA 91331, USA
Email: alam@ohio.edu

Keywords: *Fluid flow, Foam, Convection*

ABSTRACT

Recent advances in the integrated circuits require very efficient heat dissipation by heat sinks. In this paper, a heat sink design based on convection heat transfer in a silicon carbide (SiC) foam is investigated by numerical simulation using the FLUENT software. This analysis is based on a true 3D model of the foam obtained through x-ray tomography. A solid model of a heat sink is then developed by reconstructing the surface from the x-ray images, and then coolant flow through the foam is analyzed. The results of the numerical simulation confirm a large enhancement of heat transfer due the presence of the high conductivity foam.

1. INTRODUCTION

Traditional heat sinks for integrated circuits such CPUs have used finned structures that are cooled by natural or forced convection. However, the drastic increase in heat dissipation due to the high density of electronic circuits has boosted the research and development of advanced heat sinks. Metallic and non-metallic foams are being studied as flow media components in heat sinks that provide high heat dissipation. Silicon carbide foam (shown in Figure 1(a)), which have thermal expansion properties that are a compatible with electronic chips, is a potential candidate for such heat sinks. SiC foams that can be used in these heat sinks provide excellent thermal transport. While these foams do create some pressure drop, the pressure drop is far less than in graphitic foams.

The convection phenomenon of flow through foams is a complex process which is often analyzed by a homogenization process in which the properties of the foam and the flow are averaged over volume elements with hundreds of cells. In the present study, the goal is to study the fluid flow and heat transfer at the pore level in a true solid model of the foam. The solid model is developed based on x-ray tomography images, which produce a file containing a point cloud of data points. There are several steps involved in modeling and analysis of the foam. These include: (i) surface reconstruction starting from the point cloud representation of the foam, (ii) translation into solid model, and (iii) analysis by FLUENT software for numerical simulation of the flow to determine the pressure drop and heat transfer.

Based on the convection analysis, an effective heat transfer coefficient (h_{eff}) is determined. From a heat sink point of view, h_{eff} is a more useful quantity than the heat transfer coefficient from the foam surface to the fluid. This is calculated as the effective value of heat transfer coefficient at the base area that would produce same total heat transfer that was observed in the model with the foam. Another way of looking at this is that it reflects the enhancement in heat transfer at the base plate due to the presence of the foam. Since the SiC has high conductivity, it behaves as highly efficient fins. Therefore, a large enhancement in heat transfer can result from the extended surface area.

2. 3D MODELING OF SILICON CARBIDE FOAM

The 3D rendering of the silicon carbide foam was obtained by x-ray tomography which produces a 3D point cloud that resembles the geometry of the silicon carbide foam. The point cloud is used to create a solid model shown in Figure 1(b). The solid model of the silicon carbide foam is subtracted from a parallelepiped to create the fluid in the channel made by the foam pores. The assembled combination of silicon carbide foam–fluid model is used to simulate the fluid flow and heat transfer in a porous channel.

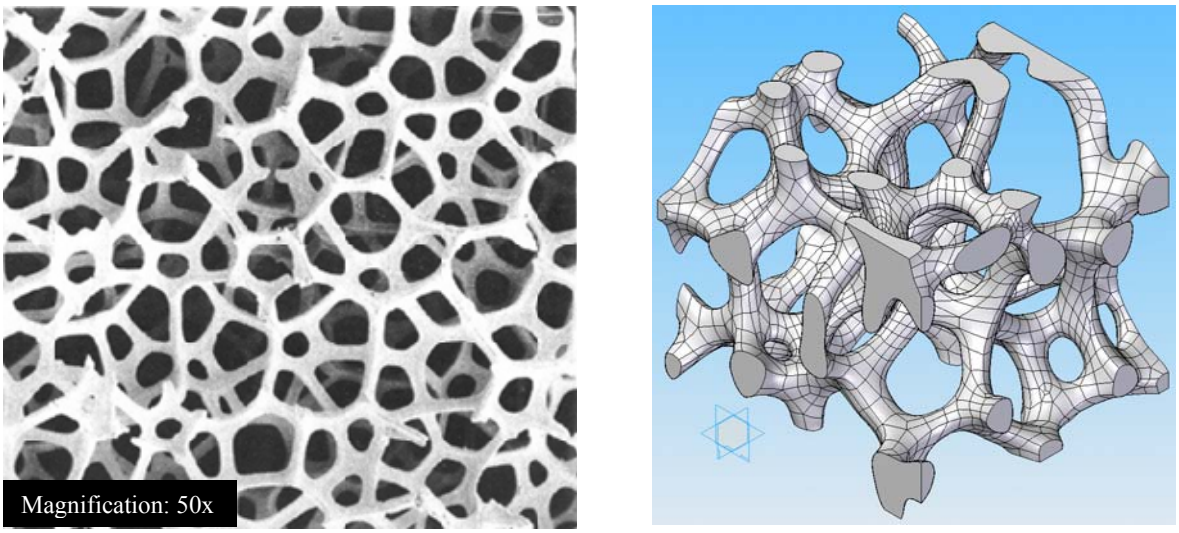

(a) (b)

Figure 1. Silicon carbide foam: (a) SEM image (Source: Ultramet) and (b) 3D solid model

The solid model assembly of the porous channel (silicon carbide foam and interstitial fluid) is meshed using tetrahedral elements in HyperMesh [1] as follows: 81,691 elements are generated for solid and 483,475 elements are generated for fluid. For the fluid flow and heat transfer analysis, a part of the solid model is utilized and symmetric conditions are used appropriately. The computational mesh is shown in Figure 2.

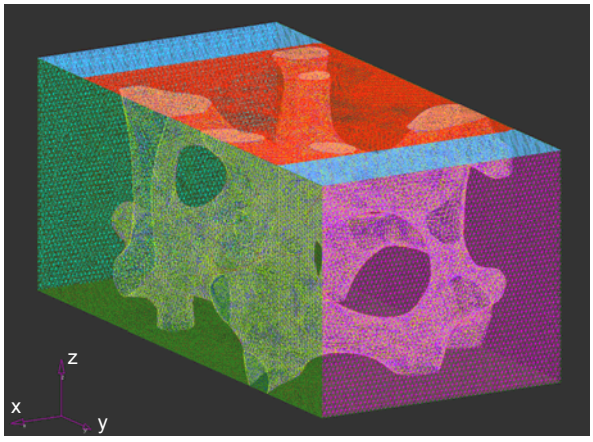

Figure 2. Computational mesh of silicon carbide foam and fluid

3. CFD ANALYSIS

The solid model of silicon carbide foam is assumed to be homogeneous and isotropic. The void fraction (porosity) of the foam is 80.7%. The system analyzed in the present research work consists of a rectangular channel filled with silicon carbide foam and saturated with coolant (water); with a heat source applied on the top surface of the channel. The coolant flows along the y axis in the positive direction (see Figure 2). The steady state fluid flow and heat transfer are analyzed using simulation on the pore level model.

The velocity and pressure fields in the fluid are governed by mass conservation and Navier-Stokes equations

$$\frac{\partial u_i}{\partial x_i} = 0$$

$$\rho u_j \frac{\partial u_i}{\partial x_j} = -\frac{\partial p}{\partial x_i} + \mu \frac{\partial}{\partial x_j}\left(\frac{\partial u_i}{\partial x_j}\right) + \frac{\partial}{\partial x_j}\left(-\overline{\rho u_i' u_j'}\right)$$

where u_i are the fluid velocities, p is the fluid pressure, μ is the fluid viscosity, and ρ is the fluid density. The fluid flow is assumed viscous and incompressible, and the fluid body forces are neglected. The last term in the Navier-Stokes equations is the Reynolds stresses and is associated with turbulence. The Boussinesq hypothesis gives the Reynolds stresses as [2]

$$-\rho\overline{u_i' u_j'} = \mu_t\left(\frac{\partial u_i}{\partial x_j} + \frac{\partial u_j}{\partial x_i}\right) - \frac{2}{3}\rho k \delta_{ij}$$

where μ_t is the turbulent viscosity, k is the turbulence kinetic energy and δ_{ij} is the Kroneker delta function. The turbulent viscosity and turbulence kinetic energy are modeled by employing the $k-\varepsilon$ method as implemented in the commercial CFD code FLUENT [3], which is used here for numerical simulation. The fluid properties are assumed constant with temperature so that the fluid flow governing equations and the energy conservation equations can be decoupled and solved independently.

The boundary conditions for fluid flow simulation are: (a) constant free stream velocity at the entrance of the porous channel, (b) zero fluid velocity on the solid surfaces (foam surface and channel top surface) and (c) symmetry on the channel sides and bottom surfaces.

The fluid flow simulations yield the velocity and pressure distributions in the fluid as a function of space coordinates x, y and z.

The Darcy-Forchheimer semi-empirical equation gives the pressure drop for fluid flow through porous media [4]

$$\frac{\Delta p}{L} = \frac{\mu}{K} u_D + \frac{\rho c_f}{\sqrt{K}} u_D^2$$

where u_D is the free stream (Darcy) fluid velocity, L is the length of the porous material in the direction of the flow and K and c_f are the porous material permeability and inertial coefficient, respectively.

The temperature fields in the foam microstructure and coolant are governed by energy conservation equations for the solid and fluid without internal heat generation

$$\rho c_p \frac{\partial}{\partial x_i}\left(u_i T_f\right) = \frac{\partial}{\partial x_j}\left(k_{eff}\frac{\partial T_f}{\partial x_j}\right)$$

$$\frac{\partial}{\partial x_j}\left(k_s \frac{\partial T_s}{\partial x_j}\right) = 0$$

where T_f is the fluid temperature, k_{eff} is the fluid effective thermal conductivity, c_p is the fluid specific heat, T_s is the solid temperature and k_s is the solid thermal conductivity.

The boundary conditions for heat transfer simulation are: (a) constant temperature on the channel top surface (foam and fluid), (b) constant fluid temperature at the channel inlet, (c) symmetry on the channel sides and bottom surfaces, and (d) temperature and heat flux continuity at the solid–fluid interface.

The energy conservation equations are solved together and yield the temperature distribution in silicon carbide foam microstructure and fluid as a function of space coordinates x, y and z. The heat transfer simulation is carried out using the fluid velocity field previously calculated. The thermal properties are evaluated at the fluid inlet temperature.

An overall energy balance is employed here to calculate effective heat transfer coefficient:

$$q = \dot{m} c_p \left(T_{out} - T_{in}\right) = h_{eff} A \Delta T_{ML}, \text{ where,}$$

$$\Delta T_{ML} = \frac{T_{out} - T_{in}}{\ln \dfrac{T_0 - T_{out}}{T_0 - T_{in}}}$$

In the above equation, q is the heat flux transferred to the fluid in the porous channel, T_{in} and T_{out} are the channel inlet and outlet fluid temperatures, h_{eff} is the effective heat transfer coefficient, A is the channel top surface area and T_0 is the constant temperature applied on the channel top surface.

4. RESULTS

The assembly mesh (see Figure 2) was exported to the CFD code FLUENT for fluid flow and heat transfer simulations. Figure 3 shows the fluid flow pathlines colored by velocity magnitude for a free stream fluid velocity of 0.05 m/s. The presence of the foam in the channel reduces the cross-sectional area available for fluid flow and increases the fluid velocity. The maximum velocity is about 4.5 times higher than the free stream velocity. There is also an increase in the turbulence. Both of these effects improve the heat transfer from the foam surface to the fluid, which is further enhanced by the extended surface area of the foam.

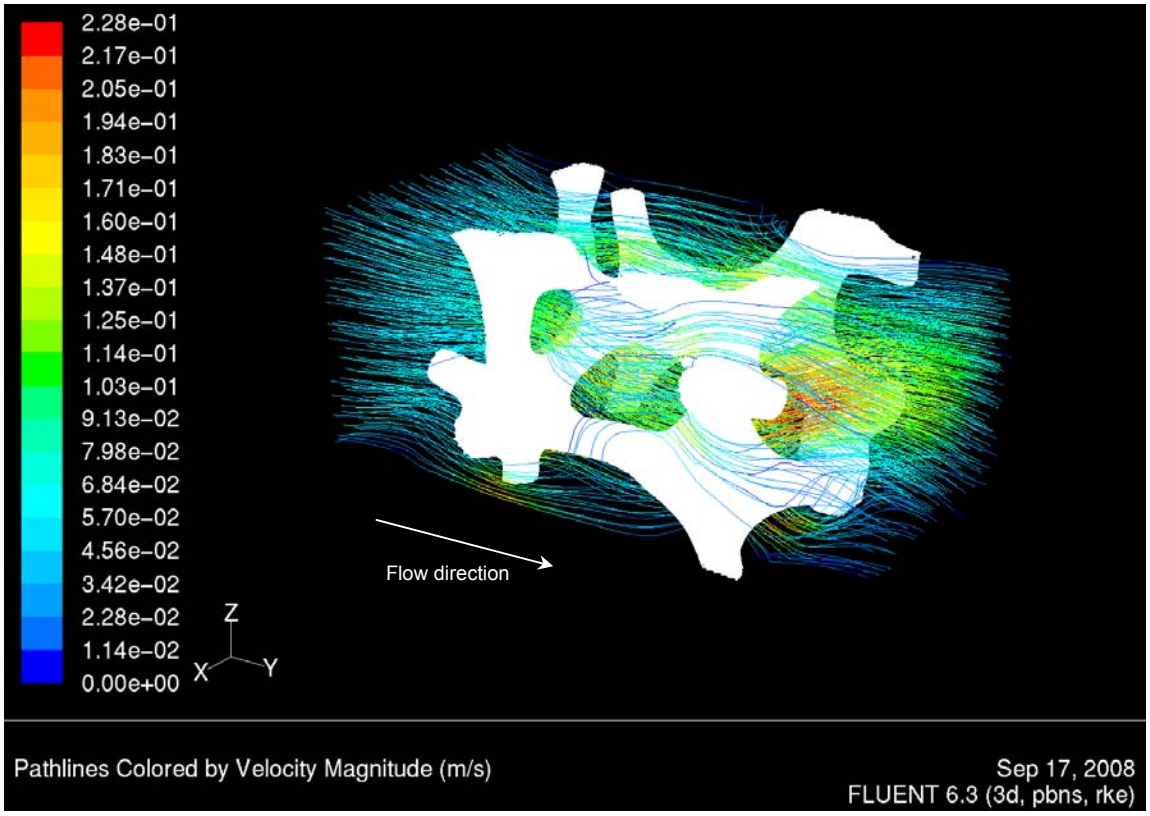

Figure 3. Fluid flow pathlines in the porous channel colored by velocity magnitude

The fluid flow simulation results are used to calculate the silicon carbide foam permeability and inertial coefficient from Darcy-Forchheimer semi-empirical equation. The simulation results of pressure drop across the foam as a function of free stream fluid velocity are shown in Figure 4. A quadratic curve is fitted through the data points in Figure 4 (top) and its equation gives the permeability value as $K = 1.107 \cdot 10^{-9}\, m^2$ and the inertial coefficient $c_f = 0.3$. The friction coefficient is also calculated from the expression introduced by Paek et al. [5]

$$f = \frac{\frac{\Delta p}{L}\sqrt{K}}{\rho u_D^2}$$

The friction coefficient as a function of modified Reynolds number ($\mathrm{Re}_K = \rho u_D \sqrt{K} / \mu$) is plotted in Figure 4 (bottom) as discrete points. In order to allow for a comparison, the experimental correlations from Paek et al. [5] and Vafai and Tien [6] are also plotted.

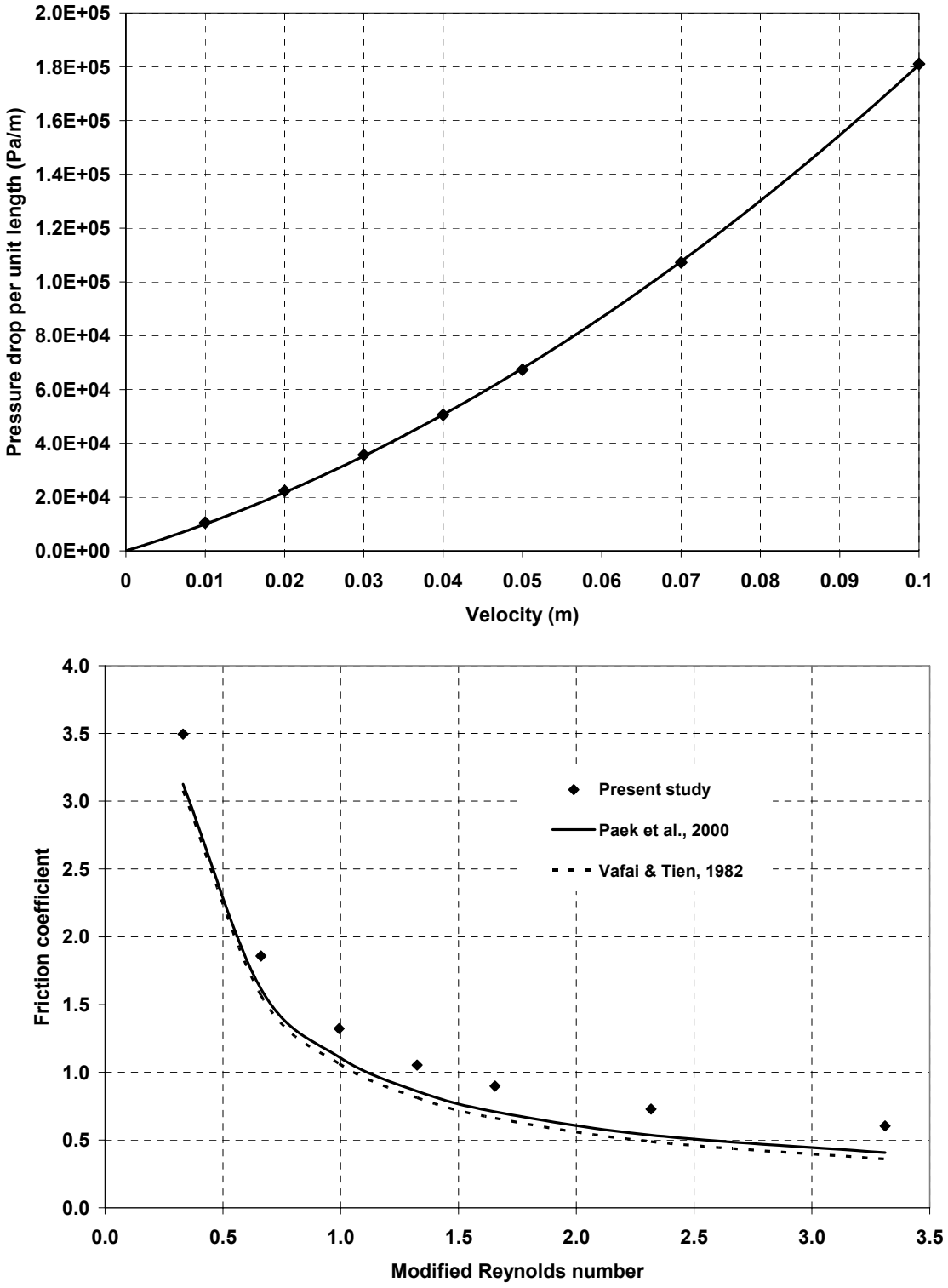

Figure 4. Pressure drop as a function of free stream velocity (top) and friction coefficient as a function of modified Reynolds number (bottom)

Figure 5 (top) shows the temperature distribution in the silicon carbide foam and in the fluid at the inlet and outlet of the channel for a free stream fluid velocity of 0.05 m/s. The most

significant feature in this figure is the low temperature gradient in the foam due to its high thermal conductivity (150 W/m°C). The foam behaves as highly efficient fins allowing for high heat transfer coefficients.

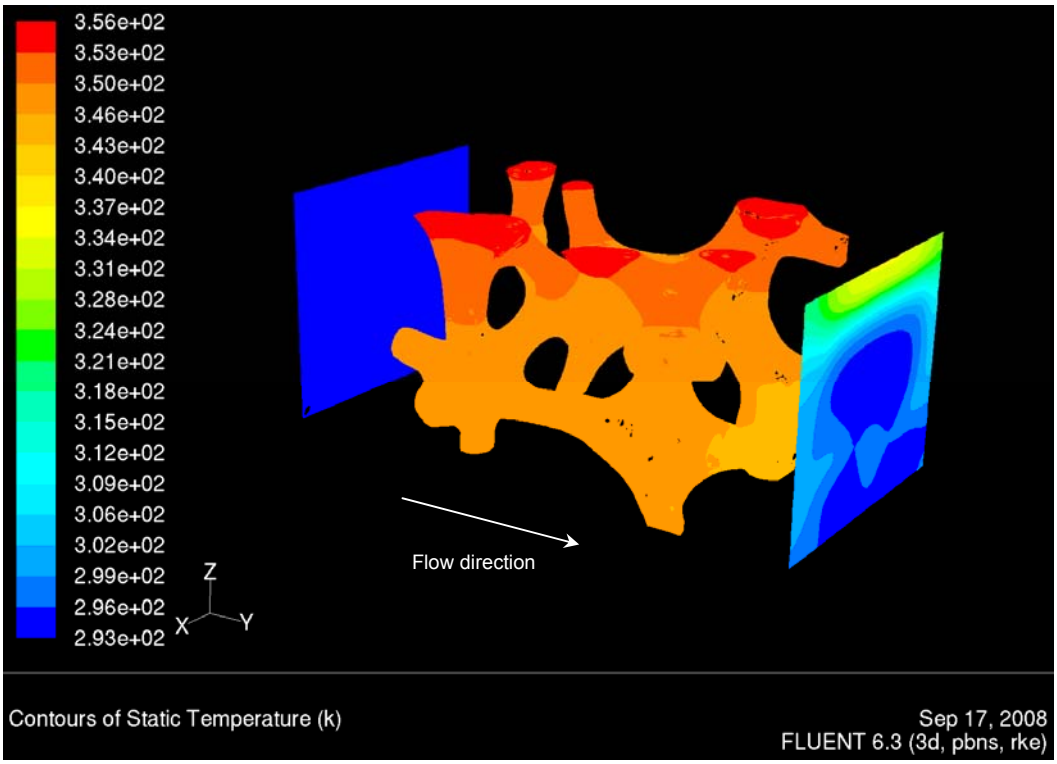

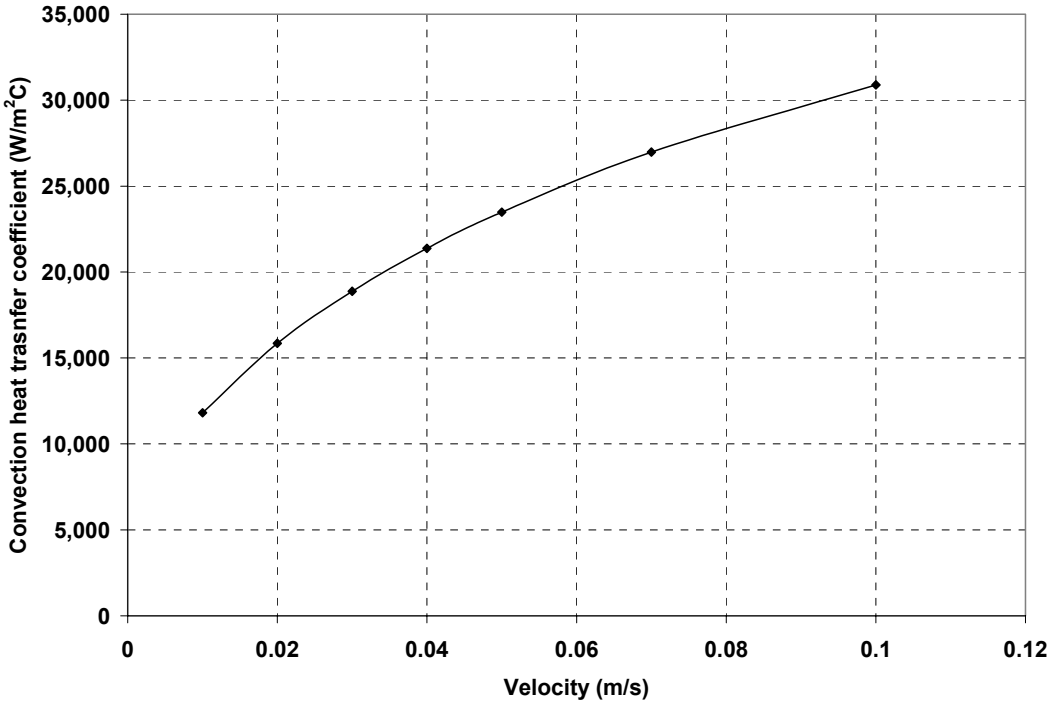

Figure 5. Temperature distribution in fluid (inlet and outlet) and silicon carbide foam (top) and effective heat transfer coefficient as a function of fluid free stream velocity (bottom)

5. CONCLUSIONS

A numerical analysis has been carried out to study the fluid flow through a foam and its effect on the heat transfer in a heat sink system. The effective heat transfer coefficient at the base of the heat sink is in the range of 12,000 to 31,000 $W/m^2°C$. This is a large enhancement that is due, in part, to the effect of the extended surface area of the foam (7,175 m^2/m^3) which results in a total surface area that is 4.3 times higher than the base area of the heat sink. The high thermal conductivity of the foam and the high surface area produce an effect of highly efficient fins. The pore geometry produces a flow path that is highly tortuous, but the windows between adjacent cells are unobstructed, so the pressure drop in the flow is not as high as observed in graphitic foams. These properties make the SiC foam a potential candidate for heat sink systems.

ACKNOWLEDGEMENT

The authors would like to acknowledge the support provided by Ultramet and use of Hypermesh and Fluent provided by Ohio Supercomputer Center for this research work.

REFERENCES

[1] Altair Engineering Inc., HyperMesh 8.0, 2007
[2] Hinze, J. O., 1975, "Turbulence" (2nd ed.), McGraw-Hill Publishing Co., NY
[3] Fluent Inc., FLUENT 6.3 User's Guide, 2006
[4] Beavers, G. S., and Sparrow, M., 1969, "Non-Darcy flow through fibrous porous media", Transactions of the ASME. Series E, Journal of Applied Mechanics, 36(4), pp. 711-714
[5] Paek, J. W., Kang, B. H., Kim, S. Y., and Hyun, J. M., 2000, "Effective thermal conductivity and permeability of aluminum foam materials", International Journal of Thermophysics, 21(2), pp. 453-464
[6] Vafai, K., and Tien, C. L., 1982, "Boundary and inertia effects on convective mass transfer in porous media", International Journal of Heat and Mass Transfer, 25(8), pp. 1183-1190

Characteristics of Time Mean Velocity and Temperature Fields for a Fully Developed Turbulent Flow in an Asymmetrically Heated Square Duct with Ribbed Rough Bottom Wall

AKM Abdul Hamid[1], M.A. Taher Ali[2] and Adur Razzak Akhanda[3]

[1] *Mechanical Engineering Department, RUET, Rajshahi-6204, Bangladesh.*

[2] *Mechanical Engineering Department, BUET, Dhaka-1000, Bangladesh.*

[3] *Department of Mechanical and Chemical Engineering, IUT, Gazipur-1704, Bangladesh.*

[1]*E-mail: mahamid_ruet@yahoo.com*

Abstract

This paper presents experimental results concerning a time mean velocity and temperature fields obtained for a fully developed turbulent flow through an asymmetrically heated square duct with bottom wall ribbed rough at constant heat flux boundary condition for ten Reynolds numbers varying within the range of $4\times10^4<Re<9\times10^4$. *The ratios rib height to mean hydraulic diameter of the duct and the rib pitch to rib height are* $e/D=0.02$ *and* $p/e=8$ *respectively. The time mean air velocity profiles near the centre show parabolic form exhibiting little or no influence of secondary flow. The stream wise flow velocity profiles, bulges towards the corner along the corner bisectors and depression from duct centre towards the side walls along wall bisectors producing saddle like shape indicating the effects of secondary flow. The bulging of velocity profile is greater near unheated top smooth wall than that of the heated bottom ribbed rough wall. This difference in peak values on velocity profile is because of increase in turbulence intensity due to existence ribbed roughen wall surface as well as the effects of heat transfer from the bottom heated wall increasing the wall friction considerably. This phenomenon combined with secondary flows on the primary velocity profiles becomes more and more prominent and the saddle shape form characterizes their influence. Also the velocity gradients near the heated bottom ribbed rough wall are higher than those near the unheated top smooth wall. The air temperature decreases at a decreases rate from the heated wall towards the centre of the duct and beyond that the temperatures remain nearly constant i.e., approximately, equal to that of inlet temperature, indicating that the heat transfer becomes almost saturated and the top half of the duct behaves as a flat plate. The plots of* Θ/Θ_c *versus* u/u_c *fall on straight lines very close to each other for the range of Reynolds number studied. This demonstrates that* Θ/Θ_c, *correlates highly with* u/u_c, *suggesting the perfect similarity between the temperature and the velocity fields. The corresponding ratios of* Θ/Θ_c *are greater than those of* u/u_c *for* $u/u_c \leq 0.85$. *The semi logarithmic plots of mean velocity and temperature show that they lie on a straight line indicating that the present experimental values obey the universal velocity and temperature distribution laws in the lower half of the duct cross-section near the heated bottom ribbed rough wall. The compact empirical correlations for universal velocity and temperature distributions for fully developed flow are obtained can be used for improved design of the heat transfer equipments for engineering applications.*

1. Introduction

Amongst the wide variety of heat transfer mechanism, forced convective heat transfer is one which is used extensively in engineering fields. Many investigators show that the flow in noncircular ducts is accompanied by secondary flow perpendicular to the stream wise flow direction. This secondary flow not only reduces volumetric flow rate but also distorts the axial velocity field which in turn distorts the temperature field, [6] and [8]. The secondary flow produces an increase in the wall shear stress towards the corners and significant influence on heat transfer at the walls. Until recently, experimental investigation of these cases was confined to comparatively simple cases with symmetrical boundary conditions. Studies of similar detail are very few in more complicated geometries with dissimilar boundary conditions, curvature and heating systems of different processes. A brief literature survey indicates the lack of reliable experimental data on related variable parameters both velocity and temperature profiles in a square duct heated asymmetrically with constant heat flux boundary condition. An experimental study on forced convective heat transfer from the square duct with bottom wall ribbed rough and heated asymmetrically has been carried out for ten Reynolds numbers varying from $4x10^4$ to $9x10^4$. The gathered data will be useful for those pursuing the task of numerical prediction in this area of research and development. The object is to provide a good understanding and to obtained compact correlations, including Prandtl number as a variable parameter that can be used for improved numerical analysis and hence for a better design of equipments for engineering applications.

2. Literature survey

In the past decades, several researchers measured the primary flow velocity and got some useful results (i.e., [2], [7], [9], [12], [13], and [21]), found that the length, required for full flow development in a pipe may exceed 140 diameters. According to this viewpoint, only in a few experiments of fully developed flow has been achieved [12]. The turbulent flows as well as the temperature field in non-circular ducts are influenced by the existence of the secondary flow, [8], and [11]. Though the velocity of this secondary flow is a small percentage of the primary flow velocity, of the order of 2 to 3 percent, its influence on the flow and temperature fields in the duct can not be ignored, [3], [6], [9], and [20]. This is the reason why these flows and temperature fields have attracted interest not only for the light they shed on fluid dynamics, but also in relation to the augmentation of heat transfer, [6] and [13].

3. Experimental set up and methodology

The experimental set up has been designed and instruments and probes are installed in it and these are connected with a high speed digital computer [1]. A schematic diagram of the straight experimental setup of length 9735 mm is illustrated in the Figure 1. The test square duct of length 5989 mm having cross section area of 50mm×50mm consists of heated section of length 1833mm (=36.66D) and unheated section of 3036mm (=60.06D). The unheated section of the duct serves to establish hydrodynamically fully developed flow at the entrance to the heated section. In order to minimize any possible end effects to be transmitted at the test sections, a smooth duct of 1120mm long having the same cross sectional dimensions as that of test duct is attached at the downstream end of the heated test section. Fig: 2 illustrates the details of the cross sectional view of the test section. Two side walls of the entire test duct are made from Bakelite sheet of 12mm thick to provide both the high strength and to ensure no leakage of current. The top wall is made from transparent plexiglass plate of thickness 12mm in order to provide optical access for observation and necessary adjustment of probes. The entire test duct except the top wall is enclosed in glass wool to minimize heat loss. The filtered air at room temperature is drawn into the straight square test duct through the air filter followed by inlet parabolic nozzle in order to establish uniform velocity. Only the bottom wall is heated electrically. To maintain a constant heat flux a voltage stabilizer followed by a voltage regulator, both having 1kW capacity is used for constant power supply to the heater. The flat nichrome wire of size 28 SWG having the resistance of 9.8097 Ω/m is used to achieve uniform wall heat flux conditions. As the thermocouple is attached intrinsically with the pitot static tube measurements of both the velocity and temperature of the air flowing through the duct are taken simultaneously. The bottom wall temperatures of the test section are measured by 8 copper constant thermocouples distributed along the entire length of the heated test duct. Thermocouples also are used to

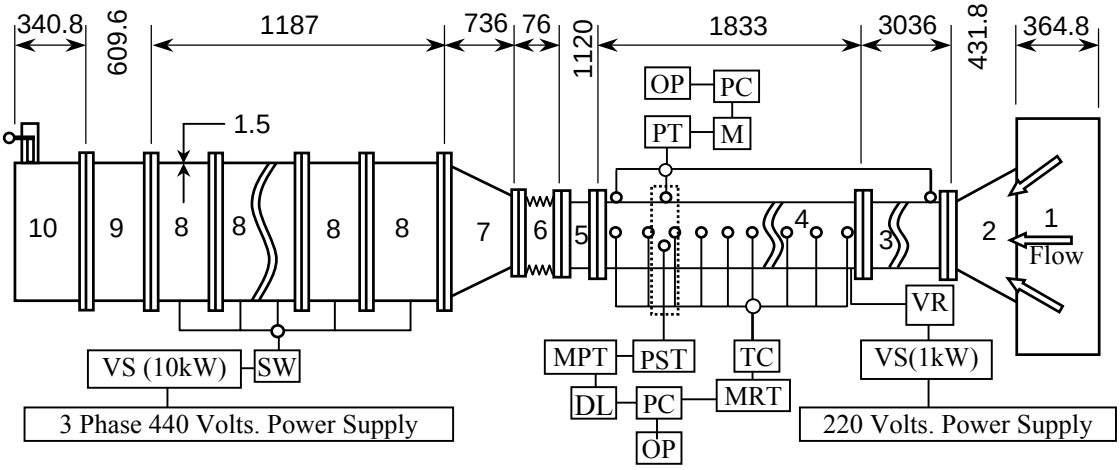

LEGEND **All Dimension are in mm**

1. Air Filter	8. Fans	9. Silencer	DL = Data Logger
2. Inlet Contractor	10. Butter Fly		PC = Personal Computer
3. Unheated Duct	TC = Thermo-couple		OP = Out-put
4. Heated Test Duct	DTR = Digital Temperature Recorder		PT = Pitot Tube
5. Unheated Duct	PST = Pilot Static Tube		SW = Switch
6. Bellow	MPT = Micro Pressure Transducer		VS = Voltage Stabilizer
7. Diffuser	M = Manometer		VR = Voltage Regulator

Fig: 1 Schematic diagram of the experimental setup

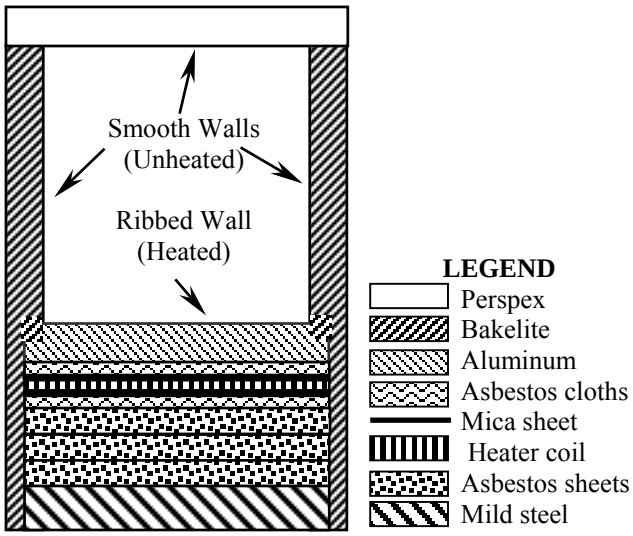

Figure 2 Illustrating cross sectional view of duct

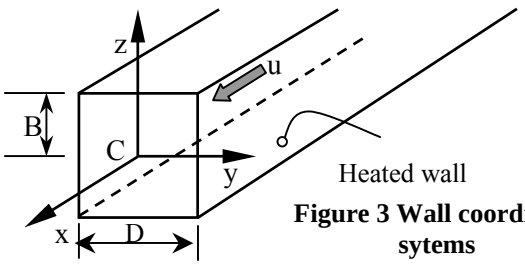

Figure 3 Wall coordinate sytems

measure the bulk mean air temperature entering and leaving the test section. Two pressure tapings (one at x=0.20D and the other at x=94.56D i.e., x=34.5D from the leading edge of the heated test section) are used for the static pressure drop measurement across the heated test section.

4. Measurement systems

The configuration, the dimensions of the test model, the flow direction, and the coordinate system are schematically shown in Figures 3 and 4. The mean velocity and the static pressure are measured by united Senser (USA) pitot static tube of 1.6 mm outer diameter with a Furnace Controls Ltd. (U.K.), pressure transducer (model MDC FC001 and FC012 and a Keithly (USA) digital micro-voltmeter with a data logger system (model 2426). The signals of the pitot static tube are transmitted to pressure transducer through 1.4 mm bore flexible tygon tubing. The signals of the digital micro-voltmeter manometer, using Kerosene of specific gravity 0.7934, for static pressure measurement. The output voltage is found to vary linearly with pressure in the measurement range. For the measurement of all signals with micro-voltmeter, integration times of about 30 seconds are used. Thermocouples are used to measure both wall and air temperature [1].

5. Data reduction

The net heat transfer rate can be calculated from

$$Q = \rho_f u_m A_c C_p (To - T_i) = G A_c (To - Ti) \quad (1)$$

$$q = Q/A_s \quad (2)$$

The local outer wall temperature T_w is read from the thermocouple output. The corrected local inner wall temperature, T_{wc} is calculated by one dimensional heat conduction Equation (3) as:

$$T_{wc} = T_w - (Q\delta/k\,A_s) \quad (3)$$

The average value of local heat transfer coefficient h is evaluated from:

$$h = q/\Delta T_{lm} \quad (4)$$

$$\text{Where, } \Delta T_{lm} = (T_o - T_i) / \ln[(T_{wc} - T_i) / (T_{wc} - T_o)] \quad (5)$$

Since the air velocity and temperature varies along the duct [1] and [16], all the physical properties of air and the related parameters are calculated at the local bulk mean air temperature, $T_b = ½(T_o + T_i)$ and local bulk mean air velocity, $u_b = ½(u_o + u_i)$ for each data recorded in space. The time mean velocity u is normalized by the mean velocity at the centre u_c as u/u_c and the temperature T is normalized as θ/θ_c.

$$\text{where, } \theta = (T_{wc} - T) \text{ and } \theta_c = T_{wc} - T_c. \quad (6)$$

Also the time mean velocity and the mean temperature are nondimensionalized by the friction velocity, u* and by the friction temperature, T^* as:

$$u^+ = u/u^* \text{ and } T^+ = (T_{wc} - T)/T^* \quad (7)$$

$$\text{where, } u^* = \sqrt{(\tau_w/\rho)} \text{ and } T^* = q/\rho C_p u^* \quad (8)$$

For any flow field, these nondimensional parameters are important criteria to indicate its characteristics. Similarly the distance measured from the bottom wall surface, Z is also nondimensionalized as:

$$Z^+ = u^* Z/\nu \quad (9)$$

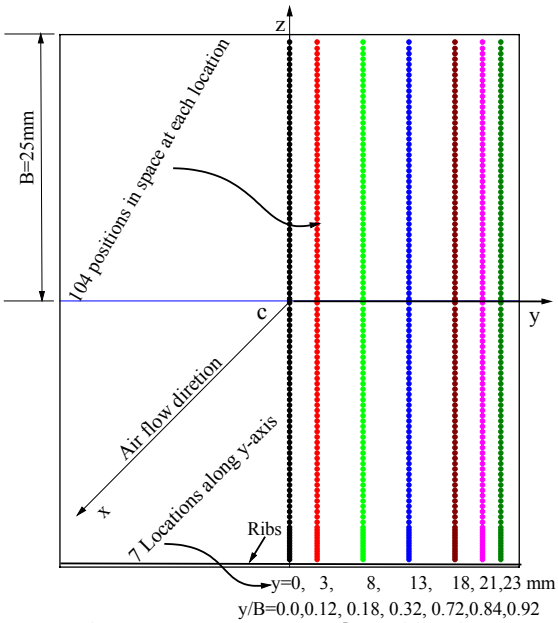

Figure 4 Dots represents probe positions in space

6. Data analysis

The top and two sides having walls and the bottom ribbed rough wall make the duct asymmetric in nature. Also the heated bottom ribbed rough wall creates flow field asymmetric. Thus duct is symmetric about z-axis but asymmetric about the y-axis. Hence the measurements are taken only in one half of the cross section about the symmetrical z-axis as shown in Figure 4. Measurements are made at the sections x=2D and x=34.5D downstream from the leading edge of the heated section i.e. at x=60D and x=94.56D respectively from the unheated section. At position x=94.5D both velocity and temperature fields can be considered to be fully developed, [16] and [17]. The time mean velocity and temperature of air are measured within the region of $-1<z/B<1$ and $0\le y/B\le 0.92$ at 7 different locations of y/B = 0.0, 0.12, 0.32, 0.52, 0.72, 0.84, and 0.92 in the cross section, Figure 4. There are typically 104 measurement points in space at each measuring location and there is a total of 104×7=728 points in space for the one half of the cross section of the duct which represents the data for the entire duct cross section, [4]. The time mean velocity and the temperature are analyzed from the probability distribution function of the measurements recorded by the data logger. The measurements are taken for 10 different Reynolds number varying between $4\times10^4<Re<9\times10^4$. In the analysis of data in the present experiment the heat transfer surface area increased by 30.37 percent is included unlike the previously published data where they ignored the surface area of ribs. In the present investigation ribs are cut down from the surface of the wall instead of attaching ribs by glow which causes thermal resistance [16]. The

present analyzes are carried out with the local values physical properties and all related variable parameters for each points in space [3] and [4]. Hence it can be said that the present experimental results obtained are more accurate and reliable.

The corresponding statistical error is between 0.51 to 2.05 percent in the time mean velocity and between 1.23 to 2.15 percent in the temperature. The scattering of the wall temperature measurement is found to be between 2.11 to 3.24 percent and the uniformity of the wall temperature distribution is considered to be satisfactory [19]. The time velocity measurements are repeated whenever error or doubtful situations occurred to ensure that the measured results are repeatable.

7. Results and discussions

The experimental results concerning a time mean velocity and temperature fields obtained for a turbulent flow through an asymmetrically heated ribbed rough square duct with constant heat flux as the boundary condition are investigated. To get the over view regarding the magnitude and the distribution of these two important parameters of the flow field the profiles are drawn and discussed briefly for the lowest and the highest Reynolds numbers only.

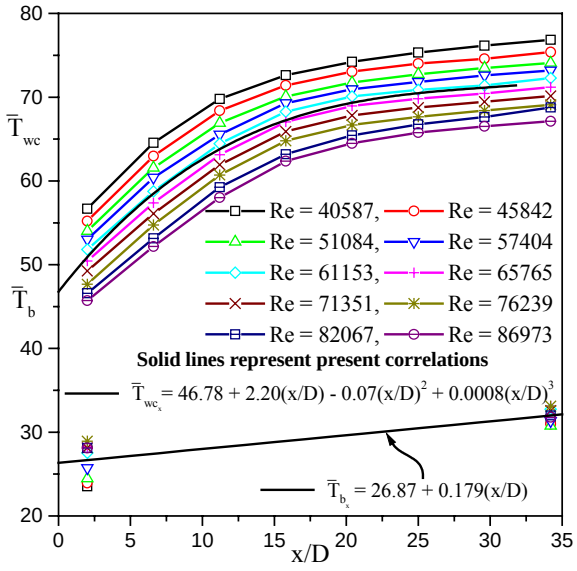

Figure 5 Wall and air temperature distributions

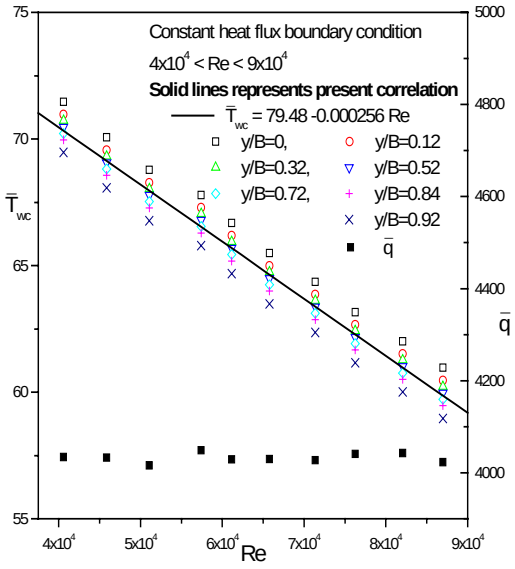

Figure 6 Effects on local wall temperature and heat flux

7.1. Wall and air temperature distributions along length of duct

Fig: 5 illustrates the distributions of local bottom wall temperature, T_w supplied along the length of the duct and the bulk mean air temperature, T_b in the duct as a function of longitudinal positions. The longitudinal distribution of the bulk mean air temperature is assumed to increase linearly as stated by many investigators, [4], [7], [15], and [16]. The longitudinally constant heat flux boundary condition of the present investigation, thermally fully developed region is characterized by wall and air temperature that increases linearly as a function of longitudinal positions. The figure shows the linear increase of bulk mean air temperature measured from the inlet to the outlet. At constant Reynolds number, the wall temperature increases at a decreasing rate approaching the asymptotic condition near x=15D and after this the longitudinal distribution of wall temperature increases linearly up to the last station of measurement at x=34.5D. The Figure 5 also shows continuous shifting of the temperature profile curve downwards with the increase of Reynolds number confirming increased heat extraction from the heated wall with the increase of flow velocity. Typically, at downstream distances from x=15D from the start of leading edge of the heating section Figure 5, the wall temperature become parallel to aforementioned bulk mean air temperature straight line. The average of the bulk mean temperature distribution and the corrected wall temperature can be expressed by the equations obtained as given bellow respectively:

$$\bar{T}_b = 26.87 + 0.179(x/D) \quad (10)$$

$$\bar{T}_{wc} = 46.78 + 2.20(x/D) - 0.07(x/D)^2 + 0.0008(x/D)^3 \quad (11)$$

Fig: 6 illustrates the effect of Reynolds number on local corrected mean wall temperature, $\bar{T}_{wc}$ and on heat flux, q. With the increase of Reynolds number the wall temperature drops linearly at each location, y according to correlation obtained as follows:

$$\bar{T}_{wc} = 7948 - 0.00023Re \quad (12)$$

Also the curve shifts downwards with increase of y/B. This phenomenon is due to the combined effects of the secondary flow as well as the turbulence intensity increases with the increase of Reynolds number which in turn increases wall friction. Hence the increase of heat extraction by flowing air causes the wall temperature to drop.

7.2. Mean velocity profiles

The velocity profiles in the region 0≤y<8, Figure 7(a) show the usual parabolic form having the maximum near the centre towards the unheated wall instead of occurring at the axis of symmetry z=0.

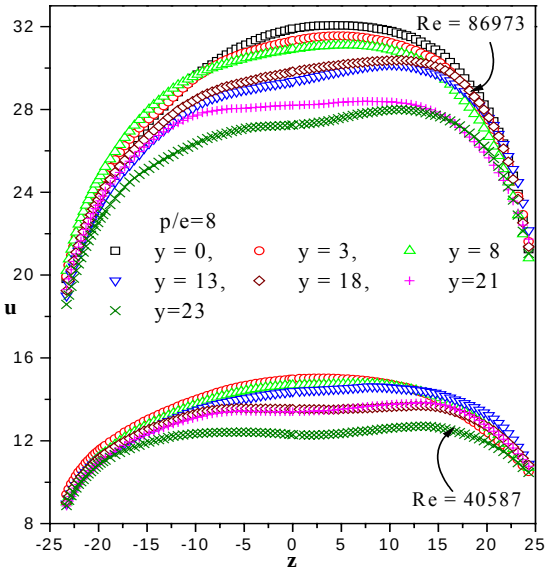

Figure 7(a) Distribution of local velocity profiles

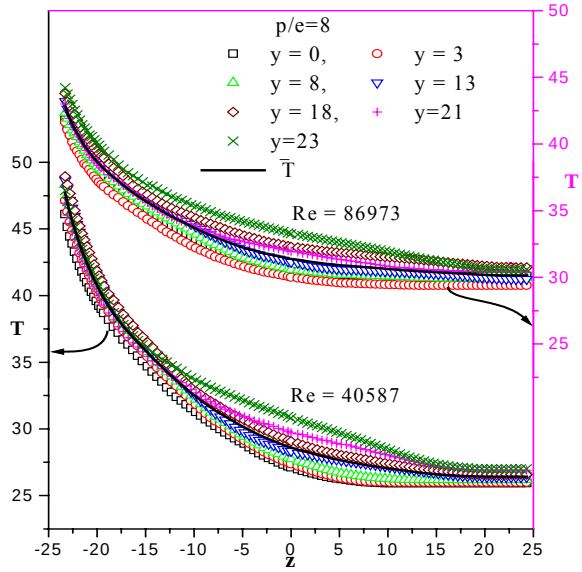

Figure 8(a) Distribution of local temperature profiles

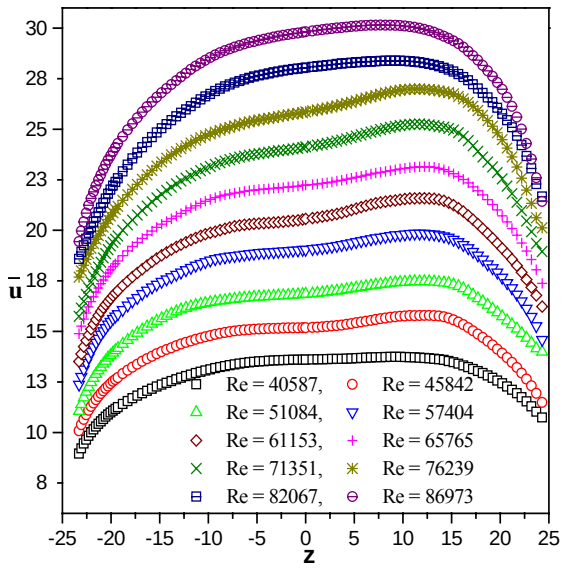

Figure 7(b) Comparison of mean velocity profile

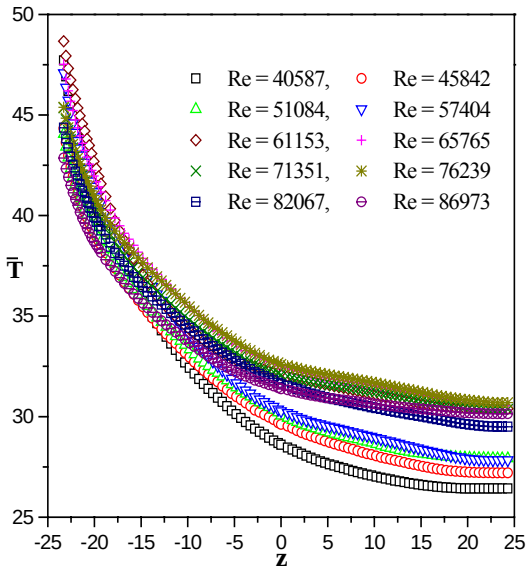

Figure 8(b) Comparison of mean velocity profile

And this peak simultaneously becomes less prominent and vanishes as the profile moves towards the sidewalls for y>8 and the profiles near the side walls show their saddle shape form. The secondary flow carries the high velocity flow from the center towards the corner increasing the velocity there, thereby creating this shape of the profiles. The velocity profiles locations y<8 are different from those near the

sidewall because of the fact that there is no bulging in these profiles indicating little influence of secondary velocity on mean axial velocity in the central region of the duct. Thus the stream wise flow velocity profiles, bulges towards the corner along the corner bisectors and depression from duct centre towards the side walls along wall bisectors producing saddle like shape indicating the effects of secondary flow. The bulging of velocity profile at each location for y>8 is greater near unheated top smooth wall than that of the heated bottom ribbed rough wall. This difference in peak values on velocity profile is because of increase in turbulence intensity due to existence ribbed roughen wall surface as well as the effects of heat transfer from the bottom heated wall increasing the wall friction considerably. This phenomenon combined with secondary flows on the primary velocity profiles becomes more and more prominent and the saddle shape form of profiles from its usual parabolic form characterizes their influence. Also the velocity gradients near the heated bottom ribbed rough wall are higher than those near the unheated top smooth wall. The temperature difference changes the viscosity of air thereby reshaping the profile and at the same time the presence secondary flow however small it is in that region, greatly influence the mean velocity profile to its final shape as found in the experiment.

Figure 7(b) shows the Comparison of average of time mean velocity profiles at constant Reynolds number. The profiles shift upward with increase of Reynolds of number. It is clearly seen that the velocity gradient is steeper near the heated bottom ribbed rough wall than that near the unheated top smooth wall as well as near the bottom wall the velocity gradients are more steeper at higher Reynolds number than that at the top wall.

7.3. Mean temperature profiles

As it can be seen from Figure 8(a) that the air entering the heated test section the temperature remains almost constant in the top half region of the duct i.e., z>0, which means that in this region the duct behaves like a flat plate. In the lower half of the duct i.e., −z<0 the temperature of air starts increasing at the increasing rate until the heated bottom ribbed rough wall where the maximum temperature is reached. The Figure 8(a) also shows that temperature profiles in the region -20<y<0 are distorted because of the combined effects on flow fields at each location of y due to strong influence of the secondary flows, enhancing turbulence intensity because of existence of ribbed roughen wall surface and the effects of heat transfer. This phenomenon increases with the increase of y>0 towards the side walls and hence more heat extraction taking place in this region. Also this effect is greater at higher Reynolds number. Figure 8(b) shows the comparison of average of mean temperature profiles for 10 different Reynolds number. It can be seen from these plots that although the variation of uncontrolled (room temperature i.e., 24.11^{O}C to 30.34^{0}C) entry temperatures is wide, the temperature profiles near the heated bottom wall merge together, which confirms the heat extraction by air from wall is saturated. At higher Reynolds number both the time mean velocity and the temperature profiles shift upwards indicating enhance transfer of momentum and energy, and hence increase of convective heat transfer coefficients with the penalty of increase in surface friction [5]. This is because the viscosity increases with the increase of the Reynolds number and location of positions, y/B from the centre of the duct towards side walls [4].

7.4. Normalized mean velocity profiles

The normalized mean velocity profiles characteristics the behaviour of the velocity field that can be compared with the other researchers more easily because these give the variation in relative terms irrespective of both magnitudes of velocity and size of the duct. Along with this comparison the analysis of these curves will be universal. As shown in Figure 9(a) corresponding profiles exhibit the similar characteristics as that of Figure 8(a) with different magnitudes of variations. Similar to Figure 8(b), the Figure 9(b) shows the comparison of average of mean velocity profiles at constant pressure drop. But in Figure 9(b), the average of the mean normalized velocity profiles for 10 different Reynolds number are shown in the water fall plot for clear view.

7.5. Normalized mean temperature profiles

The mean temperature profiles are also normalized for the reasons described above for normalized velocity profiles. The normalized mean temperature profiles at different y/B locations are shown in Figure 10(a) for the lowest and the highest Reynolds number. Normalized mean temperature profiles of smooth duct show that Θ/Θ_c increase with decreasing rate up to the center of the duct and beyond that the Θ/Θ_c of air approach to constant values to that of inlet air temperature showing negligible effect of

heating. Thus it can be said that the duct behaves like a flat plate showing the little or no effect of unheated side and top smooth walls on their shapes. Figure 10(b) shows the comparison of average of the normalized mean temperature profiles in a water fall view.

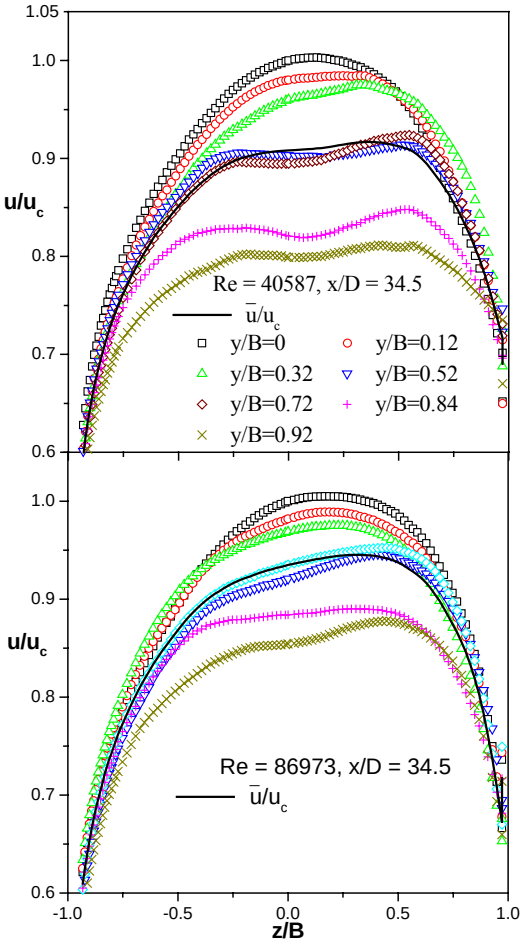

Figure 9(a) Normalized local time mean velocity profiles

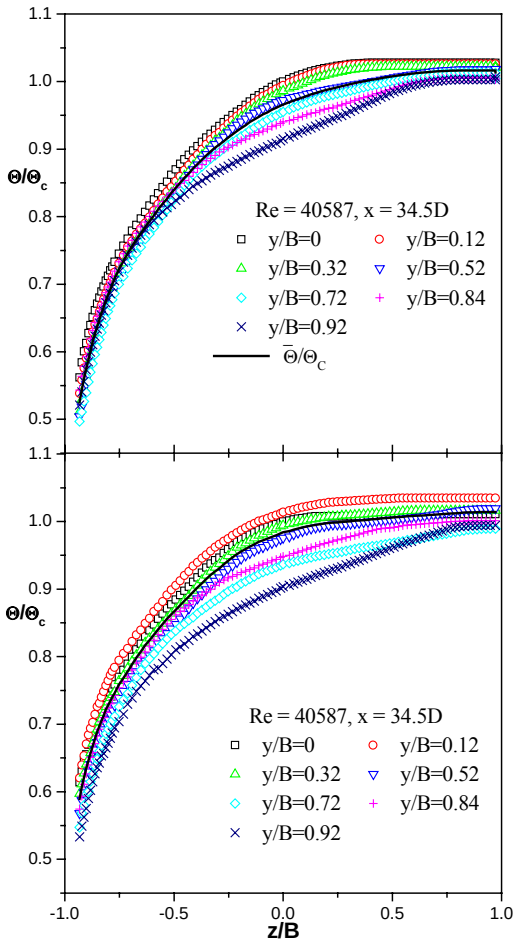

Figure 10(a) Normalized local temperature profiles

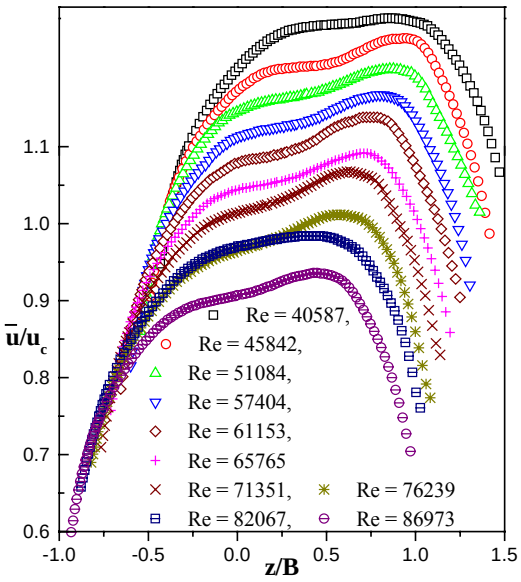

Figure 9(b) Comparison of normalized velocity profiles

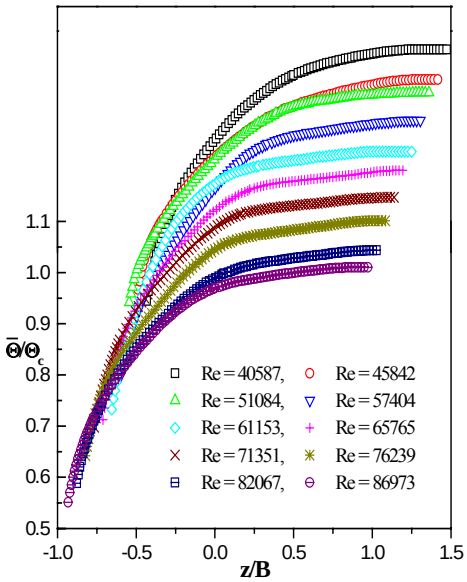

Figure 10(b) Comparison of normalized temperature profiles

7.6. Correlations between mean temperature and velocity profiles

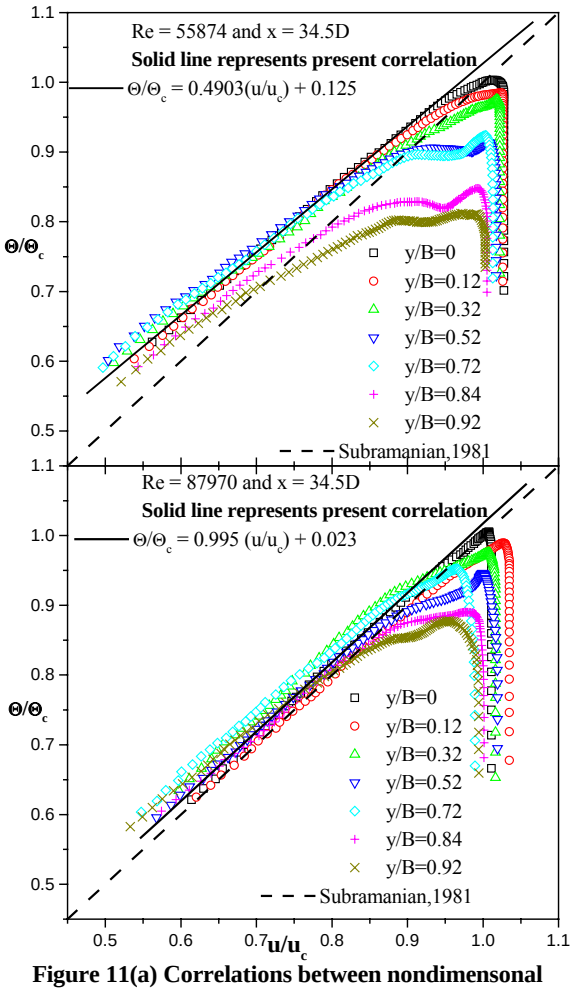

Figure 11(a) Correlations between nondimensonal local velocity and mean temperature

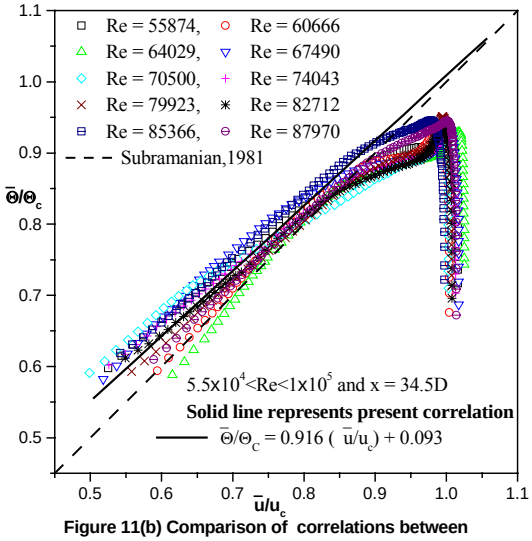

Figure 11(b) Comparison of correlations between mean velocity and mean temperature

The similarity between the nondimensional temperature and the velocity fields for the lowest and the highest Reynolds number are shown in Figure 11(a). If the temperature profile is in perfect agreement with that of velocity then the correlation follows the straight line, [22]. Accordingly, it is plausible that the more the temperature Θ/Θ_c, correlates with the velocity u/u_c, the more complete is the similarly between temperature and velocity fields, [16]. Figure 11(a) shows that the correlations curves fall on straight lines very close to each other and demonstrating high correlation between temperature and velocity fields for the range of Reynolds number studied. This demonstrates that Θ/Θ_c, correlates highly with u/u_c, suggesting the similarity between the temperature and the velocity fields. The corresponding ratios of Θ/Θ_c are greater than those of u/u_c for $u/u_c \leq 0.85$. Figure 11(a) also shows that the degree of similarity decreases with increase y/B from the centre towards side walls. Figure 11(b) shows the comparison of correlations between the temperature and velocity fields. In the present investigation the slopes of the curves ranges lie between 0.49 and 0.99. These slopes indicate the degree of similarity between the temperature and velocity fields. In a similar experiment [16] found the slope of 0.47 of similar plot for a single Reynolds number 6.5×10^4. The present values are very close to that found by [15], [16] and [23]. Though in the experiment there is no systematic increase or decrease of the slope with Reynolds number but it can be concluded from the trend of variation of slopes the temperature and velocity fields approach to perfect similarity condition. In the present investigation the correlations obtained for the lowest and the highest Reynolds number are given in the respective plots and only the average of the mean correlations for the range of Reynolds number studied is quoted as follows:

$$\Theta/\Theta_c = 0.916(\ \bar{u}/uc) - 0.093 \qquad \text{for } 40587<Re<86973 \qquad (13)$$

7.7. Universal velocity and temperature distributions

As both the time mean velocity and temperature of a heated flow field are of some polynomial function of the wall distance and wall temperature, their plots in simple linear scale shows in general, the characteristic of the flow field. The shape of the velocity profile in any ribbed rough wall flow field is greatly influenced by the wall shear stress, τ_w and the air density, ρ. This is because with the increase of

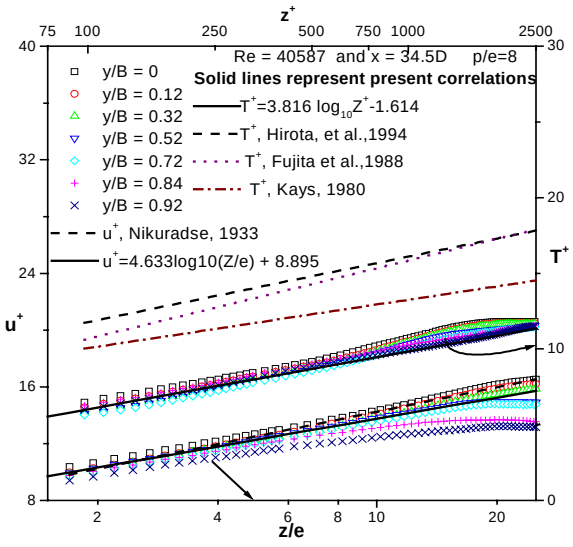

Figure 12(a) Universal local mean velocity and temperature

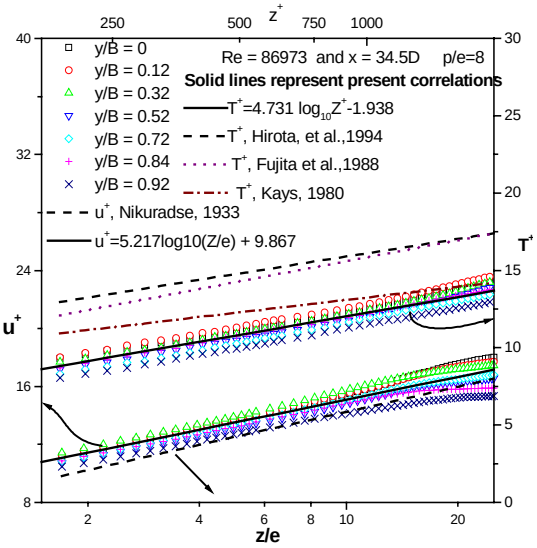

Figure 12(b) Universal local mean velocity and temperature

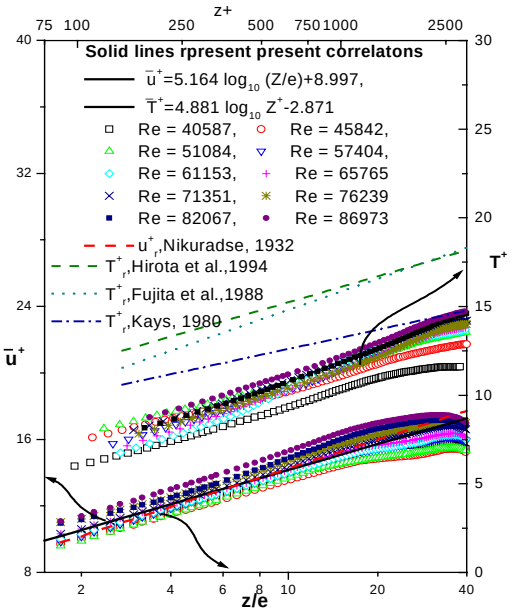

Figure 12(c) Comparison of mean universal velocity and mean temperature

air temperature the viscosity of air increases which intern increases the shear stress and the density of air decrease [4]. Thus for the same pressure difference the velocity of the air continues to accelerate with increase of air temperature. The universal velocity and temperature distributions are shown in Figures 12(a) and 12(b) for the lowest and highest Reynolds number respectively of the present investigation. In these figures experimental values for different y/B locations are, plotted and their mean values are shown by the solid lines while the broken lines represent the published data by some well known investigators as mentioned in the figures. As shown in these figures the turbulent part of the wall region $30<Z^+<250$, the mean velocity profiles are in good agreement with the logarithmic law of velocity profiles similar to published data by investigators. The generalized correlation obtained in the present investigation can be expressed by the following equation as follows:

$$u_r^+ = 5.164 \log_{10} (Z/e) + 8.997 \qquad (14)$$

The results of T^+ for each location of y/B fall on a straight line in the turbulent part of the wall region $30< Z^+ < 250$ instead of wall region $30<Z^+<200$ where the inner law is generally valid. [15] and [16]. This indicates that the inner law expressed by the logarithmic formulation is valid for the mean temperature distribution for the square duct heated asymmetrically with bottom ribbed rough wall at constant heat flux. This correlations obtained have slopes very close to published value [11], [16], and [18], except the lower value of intercepts. This variation may be due to the different experimental setup and methodology different boundary conditions, [11] and [16]. Their curves are found to be on higher level than the present work. This difference however decreases with the increase of Reynolds number for T^+. This difference in results may also be due to the fact that in their case all the four walls of their test ducts were heated while in the present experiment only the bottom wall is heated.

Figure 12(c) shows the comparison of the universal distributions of mean velocity and temperature for the range of Reynolds numbers studied. The semi logarithmic plots of mean velocity and temperature show that they lie on a straight line indicating that the present experimental values obey the universal velocity and temperature distribution laws. The figure shows the little effect of their distribution due to the variation of Reynolds number. The following generalized logarithmic law is obtained and is represented by the solid line in Figure 12(b) as follows:

$$\bar{T}_r^+ = 4.881 \log_{10} Z^+ - 2871 \qquad (15)$$

8. Acknowledgments

This is a part of PhD woks carried out at BUET, Dhaka, by the first author under the guidance of the second and third authors. The first author is grateful to BUET authorities and staffs, the panel of expert referees, especially the second author for their comments and suggestions, which led to substantial improvement of this work.

9. References

[1] Abdul Hamid, A.K.M.; 2004, “Experimental Study on Convective Heat Transfer with Turbulence Promoters”, Ph.D. thesis, Bangladesh University of Engineering and Technology, Dhaka, Bangladesh.

[2] Abdul Hamid, A.K.M.; Akhanda, M.A.R.; and Taher Ali, M.A., 2003, “An Experimental Study On Forced Convective Heat Transfer In Asymmetric Duct Flows With Periodic Turbulent Promoters.” 3rd International Conference of Mechanical Engineers and 8th Annual Paper Meet on E-Manufacturing, Mech. Engg. Division, IEB, 20-22. Paper No. 28, pages: 07-215.

[3] Abdul Hamid, A.K.M.; and Taher Ali, M.A., 2004, "Characteristics of Mean Velocity and Mean Temperature Fields for a Turbulent Flow in an Asymmetrically Heated Square Ribbed Duct." 4th International Conference of Mechanical Engineers and 9th Annual Paper Meet on E-Manufacturing, Mech. Engg. Division, IEB, 29-31, Paper No7, pp32.

[4] Abdul Hamid, A.K.M.; Taher Ali, M.A. and Akhanda, M.A.R., 2007, "Characteristics Of Air Properties And Variable Parameters For Turbulent Flow In An Asymmetrically Heated Smooth Square Duct." 7th International Conference of Mechanical Engineers - 2007

[5] Abdul Hamid, A.K.M.; Taher Ali, M.A. and Akhanda, M.A.R., 2007, " Forced Convective Heat Transfer And Friction Factor In An Asymmetrically Heated Smooth Square Duct" 7th International Conference of Mechanical Engineers – 2007

[6] Akhanda, M.A.R., 1985, “Enhanced heat transfer in forced convective boiling,” Ph.D Thesis, University of Manchester, Institute of Science and Technology.

[7] Ali, M. T., 1978, “Flow through square duct with rough ribs,” Ph.D. Thesis, Imperia College, University of London, U.K.

[8] Brundett, E., and Baines, W.D, 1964, "The Production and Diffusion of Vorticity in the Duct Flow," J. Fluid , Vol. 19, pp. 375-394.

[9] Brundrett. E. and Burroughs, P.R. 1967, "The Temperature Inner-Law and Heat Transfer for Turbulent Air Flow in a Vertical Square duct," Int. J. Heat Mass Transfer., Vol. 10 1967, 1133.

[10] Emery, A.F., Neighbors, P.K., and Gessner, F.B., 1980, “The Numerical Prediction of Developing Turbulent Flow and Heat transfer in a Square Duct.” JSME International Journal, Vol.102, pp. 51-57, 1980.

[11] Fujita, H., Yokosawa, H., Hirota, M. and Nagata, C., 1988, "Fully developed turbulent flow and heat transfer in a square duct with two rough ended facing walls", Chemical Engineering Communications, Vol. 74, pp. 95-110.

[12] Gessner, F.B., 1964, "Turbulence and Mean-flow Characteristics of Fully Developed flow in Rectangular Channels," Ph.D. Thesis, Dept. Mech. Engg. Purdue University.

[13] Gessner, F.B., and Emery, A.F., 1981, "A Length-Scale Model for Developing Turbulent Flow in a Rectangular Duct," ASME Journal of Fluids Engineering, 1981, Vol. 103, pp. 445-455.

[14] Han, J.C. Ou, S., Park, J.S., and Lei, C.K., 1989, "Augmented Heat Transfer in Rectangular Channels of Narrow Aspect Ratios With Rib Turbulators, "International Journal of Heat and Mass Transfer, Vol. 32, No. 9, pp. 1619-1630.

[15] Han, J.C., 1984, "Heat Transfer and Friction in Channels with Two Opposite Rib-Roughened Walls," ASME Journal of Heat Transfer, Vol. 106, No. 4, pp. 774-781.

[16] Hirota, M., Fujita, H., and Yokosawa, 1994, “Experimental study on convective heat transfer for turbulent flow in a square duct with a ribbed rough wall (characteristics of mean temperature field),” ASME Journal of Heat Transfer, Vol. 116, pp.332-340.

[17] Hishida, M., Nagano, Y. and Shiraki, A., 1978, "Structure of Turbulent Temperature and Velocity Fluctuations in the Thermal Entrance Region of a Pipe," Trans. Japan Soc. Mech. Eng. (in Japanese), Vol. 44, No. 385 1978, 3145.

[18] Kays, W.M., and Crawford, M.E., 1980, “Convective Heat and Mass Transfer”, McGraw-Hill, New York.

[19] Kiline, S.J., and McClintock, F. A., 1953, "Describing Uncertainties in Single-Sample Experiments," Mechanical Engineering, Vol. 75, pp. 3-8.

[20] Komori, K., Iguch, A., and Iguni, R., 1980, "Characteristics of fully developed Turbulent flow and Mass Transfer in a Square Duct." Int. Chem, Eng, 20. (2), 219-225.

[21] Melling, A., and Whitelaw, J.H., 1976, "Turbulent flow in a rectangular duct," J.Fluid Mech., Vol. 78, part 2, pp. 289-315.

[22] Subramanian, C. S., and Antomia, R. A., 1981, "Effect of Reynolds number on a slightly Heated Turbulent Boundary Layer." Int. J. Heat Mass Transf., Vol. 27No. 11, pp 2133- 2144.

10. Nomenclature

A = Area	(m^2)	Pr = Prandtl number	(Dimensionless)
B = Half of width of duct	(m)	Q = Heat transfer	(W)
C = Specific heat, Centre	($W.s/kg^OC$)	q = Heat flux	(W/m^2)
D = Hydraulic diameter of duct	(m)	Re = Reynolds' number	(Dimensionless)
e = Ribbed height	(mm)	T = Mean temperature	(^0C)
G = Mass flux	(Kg/m^2s)	T* = Friction temperature	(^0C)
H = Heat transfer coefficient	($W/(m^2\,^0C$)	T^+ = Universal temperature	(Dimensionless)
K = Thermal conductivity	($W/(m\,^0C$)	u = Time mean velocity	(m/s)
L = Length	(m)	u* = Friction velocity	(m/s)
P = Pressure	(N/m^2)	u^+ = Universal velocity	(Dimensionless)
p = Pitch	(mm)	Pr = Prandtl number	(Dimensionless)
x, y, z = Coordinate system, Fig: 3 & 4			

10.1 Greek letters

Θ = Difference between wall temperature and air temperature	$((T_w - T)^0C)$	τ = Shear stress	(N/m^2)
Θ_c = Difference between wall temperature and air temperature at centre of duct	$((T_w - T_C)^0C)$	ν = Kinematics viscosity	(m^2/s)
δ = Aluminium wall thickness	(mm)	ρ = Density	(kg/m^3)
Δ = Difference	(Dimensionless)		

10.2 Subscripts

a = Ambient temperature	f = Fluid	L = Loss	r = Ribbed rough
b = Bulk mean	i = Inlet	m = Mean	s = Smooth duct, surface
C = Centre, correct	o = Outlet	w = Wall	
lm = Log mean temperature difference			